

Mapping dust attenuation and the 2175 Å bump at kpc scales in nearby galaxies

SHUANG ZHOU,^{1,2} CHENG LI,¹ NIU LI,¹ HOUJUN MO,³ RENBIN YAN,⁴ MICHAEL ERACLEOUS,^{5,6} MALLORY MOLINA,⁷
CARYL GRONWALL,^{5,6} NIKHIL AJGAONKAR,⁸ ZHUO CHENG,¹ AND RUONAN GUO¹

¹*Department of Astronomy, Tsinghua University, Beijing 100084, China*

²*School of Physics & Astronomy, University of Nottingham, University Park, Nottingham, NG7 2RD, UK*

³*Department of Astronomy, University of Massachusetts Amherst, MA 01003, USA*

⁴*Department of Physics, The Chinese University of Hong Kong, Sha Tin, NT, Hong Kong, China*

⁵*Department of Astronomy and Astrophysics, The Pennsylvania State University, 525 Davey Lab, University Park, PA 16802, USA*

⁶*Institute for Gravitation and the Cosmos, The Pennsylvania State University, University Park, PA 16803, USA*

⁷*Department of Physics & Astronomy, University of Utah, James Fletcher Building, 115 1400 E, Salt Lake City, UT 84112, USA*

⁸*Department of Physics and Astronomy, University of Kentucky, 505 Rose St., Lexington, KY 40506-0057, USA*

Submitted to APJ

ABSTRACT

We develop a novel approach to measure dust attenuation properties of galaxies, including the dust opacity, shape of the attenuation curve and the strength of the 2175Å absorption feature. From an observed spectrum, the method uses a model-independent approach to derive a relative attenuation curve, with absolute amplitude calibrated using NIR photometry. The dust-corrected spectrum is fitted with stellar population models to derive the dust-free model spectrum, which is compared with the observed SED/spectrum from NUV to NIR to determine dust attenuation properties. We apply this method to investigate dust attenuation on kpc scales, using a sample of 134 galaxies with integral field spectroscopy from MaNGA, NIR imaging from 2MASS, and NUV imaging from Swift/UVOT. We find the attenuation curve slope and the 2175Å bump in both optical and NUV span a wide range at kpc scales. The slope is shallower at higher optical opacity, regardless of the specific star formation rate (sSFR), minor-to-major axis ratio (b/a) of galaxies and the location of spaxels within individual galaxies. The 2175Å bump presents a strong negative correlation with the sSFR, while the correlations with the optical opacity, b/a and the location within individual galaxies are all weak. All these trends appear to be independent of the stellar mass of galaxies. Our results support the scenario that the variation of the 2175Å bump is driven predominantly by processes related to star formation, such as the destruction of small dust grains by UV radiation in star-forming regions.

Keywords: galaxies: fundamental parameters – galaxies: stellar content – galaxies: formation – galaxies: evolution

1. INTRODUCTION

Interstellar dust is an important component of interstellar media, although it accounts for only a tiny fraction of the baryon mass (e.g. Rémy-Ruyer et al. 2014; Driver et al. 2018). The light emitted by stars may be absorbed or scattered by dust particles, causing dust extinction and attenuation. Dust extinction represents

the loss of starlight, which can be measured directly using resolved sources, such as stars with known intrinsic spectra. Limited by telescope resolution, such measurements can be achieved only for the Milky Way (MW; Fitzpatrick 1999) and a few nearby galaxies, such as the Large Magellanic Cloud (LMC, Gordon et al. 2003), the Small Magellanic Cloud (SMC, Gordon & Clayton 1998) and M31 (e.g. Clayton et al. 2015). For distant galaxies, however, the redistribution of their spectral energy distribution (SED) due to dust attenuation is much more complex. The shape of the dust attenuation curve (i.e., attenuation as a function of wavelength) depends

on both the intrinsic properties of dust particles and the distributions of the dust and stellar contents along the line of sight (see Calzetti 2001 for a review). To get the intrinsic SED of a galaxy, one must carefully model the effects of dust and make proper correction for them. So far, the attenuation curve that should be used in the correction has not been identified and remains elusive in observational studies of galaxy spectra.

Calzetti et al. (1994, 2000) analysed a sample of local star burst galaxies and derived an average attenuation curve, often referred to as the Calzetti attenuation curve. Charlot & Fall (2000) proposed a two-component dust model characterized by an attenuation curve that is proportional to $\lambda^{-0.7}$ but with different optical depth for star-birth clouds and diffuse interstellar media (ISM), in order to reproduce both the infrared/ultraviolet luminosity ratio and the ultraviolet (UV) spectral slope. Both the Calzetti and Charlot & Fall (2000) curves have similar shapes in the optical band and both have been widely adopted in spectral and SED analysis of galaxies. However, there are a number of unsolved problems, especially when near ultra-violet (NUV) observations are taken into account in the analysis. For example, observations of the Milky Way (MW) show a strong absorption feature at the rest-frame wavelength around 2175Å (e.g. Cardelli et al. 1989; Fitzpatrick 1999), which is often referred to as the 2175Å bump. Similar absorption features, although with varying strength, are also seen in several local galaxies, such as LMC (Gordon et al. 2003) and M31 (e.g. Clayton et al. 2015). However, this feature appears to be negligible in the sample of starburst galaxies used by Calzetti et al. (1994).

Large multi-band surveys conducted in the past two decades have allowed statistical analyses of the 2175Å attenuation feature using large samples of galaxies (see the review by Salim & Narayanan 2020). At low redshifts, most of the studies have relied on photometry due to the lack of rest-frame UV spectra. For instance, Conroy et al. (2010) analyzed a sample of disk-dominated star-forming galaxies with photometry available in both UV from the Galaxy Evolution Explorer (*GALEX*; Martin et al. 2005) and optical from the Sloan Digital Sky Survey (SDSS; York et al. 2000). They found that the Calzetti curve provides poor fits to ultraviolet colors for moderately and highly inclined galaxies, and they speculated that the existence of the 2175Å bump is responsible for the observed trends in their galaxies. Using the near-infrared photometry from the UKIRT Infrared Deep Sky Survey-Large Area Survey (UKIDSS-LAS; Lawrence et al. 2007) and emission lines from the SDSS spectroscopic survey, in combination with *GALEX* and SDSS photometric data, Wild et al. (2011) found some

evidence for the existence of the UV absorption feature in low-redshift star-forming galaxies. In contrast, Battisti et al. (2016) found no evidence for the 2175Å feature from a sample of $\sim 10,000$ local star forming galaxies from SDSS and *GALEX*. More recently, Salim et al. (2018) derived dust attenuation curves by applying the SED fitting code *CIGALE* to $\sim 230,000$ star-forming galaxies with photometry from *GALEX*, SDSS, and the Wide-field Infrared Survey Explorer (WISE; Wright et al. 2010). They found that the dust curves of individual galaxies have large variances, but that the average curve is similar to that given by Conroy et al. (2010) and that the average UV bump strength is about one third of the MW value.

At higher redshifts where the rest-frame NUV falls in the optical, analyses of the UV absorption feature can be carried using photometric and spectroscopic data in the optical band. For instance, a series of studies of massive star forming galaxies at $1 < z < 2.5$ indicated the existence of a UV bump of moderate strength (Noll & Pierini 2005; Noll et al. 2007, 2009b). A later study by Buat et al. (2011, 2012) also suggested that a UV bump with a strength $\sim 35\%$ of the MW value is needed to model the SED of star forming galaxies at $1 < z < 2.2$. Kriek & Conroy (2013) detected the presence of a UV bump using a sample of galaxies at $0.5 < z < 2.0$, and found a correlation between the bump strength and the slope of the attenuation curve. Scoville et al. (2015) reported a UV bump feature in galaxies at even higher redshifts ($z \sim 2-6.5$). More recent studies based on different surveys (Reddy et al. 2015; Leja et al. 2017; Shivaeei et al. 2020; Barišić et al. 2020; Battisti et al. 2020; Kashino et al. 2021) generally yielded results that are consistent with the existence of the bump, with the exception of Zeimann et al. (2015), but the bump strengths obtained from different samples seemed to vary significantly.

Despite of a long history of investigation (e.g. Stecher 1965; Savage 1975; Joblin et al. 1992; Beegle et al. 1997), the dust species that dominates the bump at 2175Å is still under debate (Bradley et al. 2005; Papoular & Papoular 2009; Steglich et al. 2010). The fact that the UV bump strength in observed dust attenuation curves vary from galaxy to galaxy indicates either that those galaxies are intrinsically different in dust particle properties, or that the differences are caused by radiative transfer effects in a complex star-dust distribution in galaxies. Analyses of the evolution of the distribution of dust grains (e.g. Asano et al. 2013, 2014; Hirashita 2015) indicated that the 2175Å bump strength may be linked to the relative abundance of small dust grains in galaxies, while the lack of a 2175Å bump in starburst galaxies may be explained by the destruction of such grains (Fischera

& Dopita 2011). On the other hand, models incorporating radiative transfer effects and stellar-dust geometry (e.g. Gordon et al. 1997; Witt & Gordon 2000; Seon & Draine 2016; Narayanan et al. 2018) suggest that the dust attenuation curve is shallower as the 2175Å bump weakens (thus more similar to the Calzetti curve), and the dependence becomes stronger as the optical depth increases. Spatially resolved observations down to scales of star-forming regions and covering both optical and UV bands are needed to better understand the driving processes for the variation of the dust attenuation curve in galaxies.

In this paper we investigate the dust attenuation for a sample of 134 galaxies in the local Universe, using optical integral-field spectroscopy from the Mapping Nearby Galaxies at Apache Point Observatory (MaNGA; Bundy et al. 2015) survey, NUV photometry obtained by *Swift*/UVOT (Roming et al. 2005), and NIR photometry from the Two-Micron All Sky Survey (2MASS; Skrutskie et al. 2006). Different from previous studies based either on the global photometry of galaxies or on single-fiber spectroscopy limited to the central part of galaxies, MaNGA provides spatially-resolved spectroscopy to investigate dust attenuation down to kpc scales in individual galaxies, thus effectively reducing the influence of dust distribution in galaxies. By combining MaNGA, *Swift*/UVOT and 2MASS data, not only can we resolve dust attenuation spatially, but also probe it over a wavelength range from NUV to NIR. In addition, our method takes advantage of a newly developed technique (Li et al. 2020) which estimates the relative attenuation curve from spectral fitting without the need of assuming a functional form for the attenuation curve. Here we extend the technique by calibrating the absolute amplitude of the attenuation curve with NIR photometry, and by incorporating the UV photometry from *Swift*/UVOT to study the bump around 2175Å in the dust curve. This method provide measurements not only for the UV bump strength, but also for the slope of the attenuation curve in both the optical and UV bands. The relatively large sample also allows us to statistically study the correlation of dust properties and their dependence on star formation rate.

The paper is organized as follows. We describe our data in §2, and present the method used to estimate dust attenuation curves in §3. We present our results in §4, and our discussion in §5. Finally we summarize in §6. A standard Λ CDM cosmology with $\Omega_\Lambda = 0.7$, $\Omega_M = 0.3$ and $H_0 = 70 \text{ km s}^{-1} \text{ Mpc}^{-1}$ is assumed throughout the paper.

2. DATA

2.1. MaNGA

As one of the major experiments of the fourth-generation SDSS project (SDSS-IV; Blanton et al. 2017), MaNGA has successfully obtained integral field spectroscopy (IFS) for 10,010 nearby galaxies during the period from July 2014 through August 2020 (Bundy et al. 2015). The IFS data are obtained with integral field units (IFUs) with various sizes. Each IFU is a hexagonal-formatted fiber bundle made from 2''-core-diameter fibers with 0.5'' gaps between adjacent fiber cores. When combined with the seeing, they can provide IFS datacubes with an effective spatial resolution that can be described by a Gaussian with a full width at half maximum (FWHM) of $\sim 2.5''$ (Drory et al. 2015; Law et al. 2015). The IFU fibers are fed to the two dual-channel BOSS spectrographs on the Sloan 2.5-metre telescope (Gunn et al. 2006; Smee et al. 2013) to obtain MaNGA spectra in a wavelength range from 3622Å to 10354Å with a spectral resolution of $R \sim 2000$. With a typical exposure time of about three hours, the observational data reach a r -band signal-to-noise (S/N) of 4-8 per Å per 2'' fiber at 1-2 effective radii (R_e) of galaxies,

MaNGA galaxy targets are selected from an updated version of the NASA Sloan Atlas catalogue (NSA¹; Blanton et al. 2011). Three samples are selected: Primary, Secondary, and Color-Enhanced samples. As the main samples of the survey the Primary and Secondary samples have a flat distribution in the K -corrected i -band absolute magnitude (M_i) with the assigned IFUs covering out to 1.5 and 2.5 R_e of the galaxies, respectively. The Color-Enhanced sample additionally selects galaxies on the $NUV - r$ versus M_i diagram that are not well sampled by the Primary and Secondary samples. Overall, these samples cover a wide range of stellar mass ($10^9 M_\odot \lesssim M_* \lesssim 6 \times 10^{11} M_\odot$) and a redshift range of $0.01 < z < 0.15$, with a median redshift $z \sim 0.03$ (Wake et al. 2017). MaNGA raw data are reduced with the Data Reduction Pipeline (DRP; Law et al. 2016, 2021) to produce a datacube for each galaxy with a spaxel size of $0.5'' \times 0.5''$. The absolute flux calibration of the MaNGA spectra is better than 5% for more than 80% of the wavelength range. The flux calibration, MaNGA survey strategy and data quality tests are described in detail by Yan et al. (2016a) and Yan et al. (2016b). In addition, the MaNGA Data Analysis Pipeline (DAP; Westfall et al. 2019; Belfiore et al. 2019) provides measurements of stellar kinematics, emission lines and spec-

¹ <http://www.nsatlas.org/>

tral indices, obtained by performing full spectral fitting to the DRP datacubes. All the MaNGA data, including DRP and DAP products of the 10,010 galaxies, are released as part of the final data release of SDSS-IV (DR17²; Abdurro’uf et al. 2022).

2.2. *SwiM*

We use the *Swift*/UVOT+MaNGA (SwiM) value-added Catalog (Molina et al. 2020b) which includes 150 galaxies with public MaNGA data released with the SDSS Data Release 15 (Aguado et al. 2019) and NUV imaging data from the *Swift*/UVOT NUV archive as of April 26, 2018. The Ultraviolet Optical Telescope (UVOT; Roming et al. 2005) is one of the three instruments on the *Swift* Gamma-ray Observatory. It has a $17' \times 17'$ field-of-view (FOV) and operates in the wavelength range of 1600–8000Å. Imaging data are taken in three NUV bands: *uvw2*, *uvm2* and *uvw1* centered at 1928, 2246 and 2600Å respectively, with a point spread function (PSF) of around 2.5'' that is similar to the MaNGA spatial resolution. Note that the *uvm2* filter is centered near the 2175Å bump feature as seen in the Milky Way dust curve, making it suitable for the investigation of such a feature (see subsection 3.2). All the 150 galaxies in the SwiM catalog have data from MaNGA and in the *uvw1* and *uvw2* bands, and 134 of them also have data in the *uvm2* band. As detailed by Molina et al. (2020b), all the *Swift*/UVOT images are reprocessed carefully. For each galaxy the *Swift*/UVOT images in *uvw1* and *uvm2* and the MaNGA datacube are convolved and resampled to match the spatial resolution and spatial sampling in the *uvw2* band that has the coarsest PSF (2.92'' FWHM) and a pixel size of 1''. Molina et al. (2020b) found that the distribution of SwiM galaxies in color, effective radius and axial ratio is similar to that of the MaNGA sample, but is slightly biased for the population of low stellar mass and low star formation rate. The reader is referred to Molina et al. (2020b) for more details about the SwiM catalog. A subset of 29 galaxies in the SwiM catalog has been used to study the UV stellar attenuation and optical nebular attenuation (Molina et al. 2020a) as well as the relationship between the infrared excess (IRX) and the UV spectral index Duffy et al. (2023) in kpc-sized star forming regions. Here we consider all the 134 galaxies that have data in all the three NUV bands, thus including both star-forming and quiescent galaxy populations.

2.3. 2MASS

We also use near-infrared images from the 2MASS (Skrutskie et al. 2006). We retrieved Ks-band atlas images of the 134 SwiM galaxies from the 2MASS data Archive. The 2MASS images have the same sampling (1'' per pixel) and a very similar PSF (~ 2.5 -3.5'' FWHM) in comparison to the SwiM catalog (see above). We tried to convolve images from the three UVOT bands and the 2MASS Ks band so that they all match the lowest resolution among them. Since the spatial resolutions are not very different, the flux differences in pixels before and after the convolution are typically less than 1%, much smaller than observational uncertainties. We thus decide to simply re-sample the 2MASS images to match the spatial sampling of the SwiM images, without performing additional resolution matching.

3. METHODOLOGY

We estimate dust attenuation properties for each spatial pixel (spaxel) of our galaxies. These include (1) an absolute dust attenuation curve in the optical, $A_{\text{opt}}(\lambda)$, (2) the slope of the attenuation curve in NUV as defined by the ratio of the attenuation between the *uvw2* and *uvw1* bands, A_{w2}/A_{w1} , and (3) the 2175Å bump, characterized by the extra attenuation at 2175Å due to the bump (A_{bump}) and the strength of the bump (B). We obtain these measurements in two successive steps. First, we obtain $A_{\text{opt}}(\lambda)$ as well as a dust-free model spectrum covering the full wavelength range from NUV to NIR, using the MaNGA spectrum and the Ks band photometry in the spaxel. Next, the dust-free model spectrum in the NUV is combined with the *Swift*/UVOT photometry in *uvw2*, *uvm2* and *uvw1* to estimate A_{w2}/A_{w1} , A_{bump} and B . In the rest of this section, we describe the two steps in detail and test our method with a set of mock spectra.

3.1. Deriving the optical attenuation curve and the dust-free model spectrum

For a given spaxel of each galaxy, we start by applying the technique of Li et al. (2020) to the MaNGA spectrum to estimate a relative attenuation curve in the optical range, $A_{\text{opt}}(\lambda) - A_V$, where A_V is the dust attenuation in the V-band. The attenuation curve is then used to correct the effect of relative attenuation in the observed spectrum, resulting in a dust-free spectrum but with an arbitrary flux unit. Next, a spectral fitting code, Bayesian Inference of Galaxy Spectra (BIGS; Zhou et al. 2019), is applied to the dust-free spectrum to obtain a best-fit model spectrum covering the full wavelength range from NUV to NIR. Finally, this model spectrum is flux calibrated using the Ks band photometry which is assumed to be unaffected by the dust.

² <https://www.sdss.org/dr17/manga/>

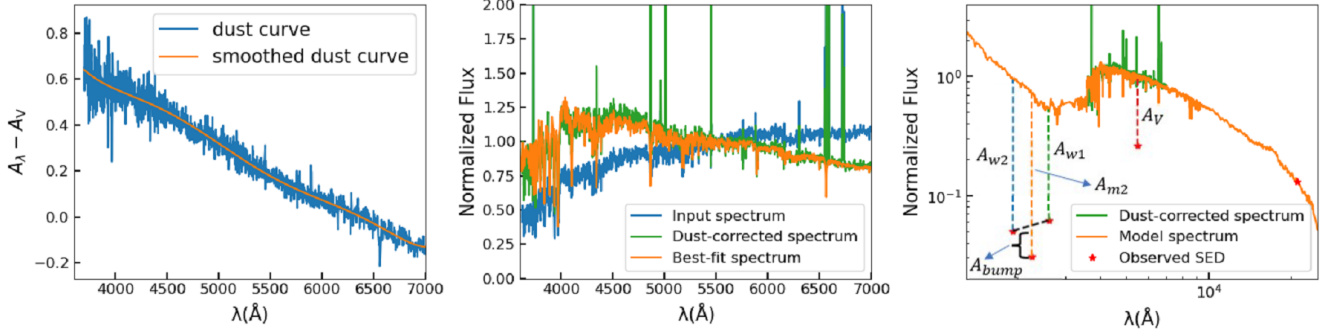


Figure 1. Illustration of the method used in this work. The blue line in the middle panel is one spectrum stacked within 1Re of our sample galaxy. In the plot we normalized the spectrum at 5500Å. We use the method of Li et al. 2020 to fit the spectrum and correct for the dust attenuation in optical range. The method of Li et al. 2020 will give a relative attenuation curve, which is shown in the left panel. After correcting for the dust attenuation, we fit the corrected spectrum with the spectrum fitting code BIGS. As shown in the right plot, the best-fit spectrum provided by BIGS is extended to both NUV and NIR (orange line). This dust-free spectrum is convolved with filter response functions to predict dust-free SED, which is compared with the observed SED shown by red stars in the right plot. By assuming that the Ks band is not affected by dust attenuation, the observed SED is also normalized so that the flux at Ks band is the same as the dust-free spectrum. The difference between the dust-free SED and observed SED is our attenuation estimation, which is indicated as dash lines in the right panel.

The detail of our method to estimate $A_{\text{opt}}(\lambda) - A_V$ can be found in Li et al. (2020). In short, for a given spectrum, this method first decomposes it into two components: one representing small-scale features of the spectrum (S) and one describing the large-scale spectral shape (L). The large-scale component L is obtained by applying a moving average filter:

$$F_L(\lambda) = \frac{1}{\Delta\lambda} \int_{\lambda-\Delta\lambda/2}^{\lambda+\Delta\lambda/2} F(\lambda') d\lambda', \quad (1)$$

where F and F_L are the original spectrum and the L component respectively, and $\Delta\lambda$ specifies the size of the wavelength window of the filter. The spectrum of the small-scale component is then given by

$$F_S(\lambda) = F(\lambda) - F_L(\lambda). \quad (2)$$

This decomposition is performed for both the observed spectra and the spectra of all the simple-stellar-population (SSP) models of Bruzual & Charlot (2003, hereafter BC03). As shown in Li et al. (2020) (see §2.1 and Eqns. 3-8 in that paper), the two components are attenuated by dust in the same way and so their ratio S/L is expected to be free of dust attenuation, as long as dust attenuation curves are similar for different stellar populations or the optical depths are smaller than unity. Therefore, the intrinsic dust-free spectrum of the stellar populations in a given spaxel can be derived by fitting the S/L of the observed spectrum to the S/L of the SSP models. The relative attenuation curve $A_{\text{opt}}(\lambda) - A_V$ is then obtained by comparing the observed spectrum with the best-fit model spectrum. One important advantage of this method is that $A_{\text{opt}}(\lambda) - A_V$ can be obtained directly for the entire wavelength range of the observed

spectrum without the need of assuming a functional form for the curve. Extensive tests on mock spectra in Li et al. (2020) showed that the method can accurately recover the input attenuation curves. The method produces unbiased estimates of the average $E(B - V)$ for spectra of various S/N and $E(B - V)$ values. The standard deviation of $E(B - V)$ obtained from individual spectra is relatively small, and decreases from ~ 0.1 mag for spectra of S/N= 5 down to < 0.03 mag for S/N larger than 20 (see Fig.7 of Li et al. 2020). We note that an uncertainty of 0.03 mag in $E(B - V)$ induces an uncertainty of ~ 0.1 mag in A_V for the Calzetti attenuation curve. In what follows we use spaxels with S/N > 20 in MaNGA.

Figure 1 (the leftmost panel) shows the relative attenuation curve obtained this way for an example spaxel in our sample. As can be seen, the curve inherits all the noise features from the observed spectrum³. We fit the curve with a polynomial to obtain a smooth curve (plotted as the yellow line in the figure), which is then used to correct the dust attenuation effect in the observed spectrum. The middle panel of the same figure displays both the observed and the dust-corrected spectra, as well as the best-fit model spectrum obtained by applying BIGS to the dust-corrected one.

In fitting the dust-corrected spectrum, we follow our previous studies (Zhou et al. 2020, 2021) and use a Γ +B model to characterize the star formation history (SFH).

³ Note that emission lines are masked out from the observed spectrum so they are not present in the attenuation curve; see Li et al. 2020 for details.

In this case, a Γ function is adopted to describe the long-term history of star formation rate over cosmic time:

$$\Psi(t) = \frac{1}{\tau\gamma(\alpha, t_0/\tau)} \left(\frac{t_0 - t}{\tau}\right)^{\alpha-1} e^{-(t_0-t)/\tau}, \quad (3)$$

where α and τ are free parameters determining the overall shape of the SFH, t_0 is the present-day time (i.e. the age of the universe, assumed to be 14Gyr), $t_0 - t$ is thus the look-back time, and $\gamma(\alpha, t_0/\tau) \equiv \int_0^{t_0/\tau} x^{\alpha-1} e^{-x} dx$ normalizes the SFH over the age of the universe. An additional burst component characterised by a SSP with the burst time being a free parameter is added to account for possible bursty events in the history. Having been recently used to explore the SFHs of low mass galaxies (Zhou et al. 2020) and massive red spirals (Zhou et al. 2021) in MaNGA, this model has shown substantial robustness and flexibility. The SFH model is combined with the BC03 SSP model spectra assuming a stellar initial mass function (IMF) of Chabrier (2003) to generate composite model spectra with various model parameters (coefficients of SSPs, α , τ , etc.). Each model spectrum is then convolved with the stellar velocity dispersion derived above from the procedure of deriving the relative attenuation curve to account for stellar kinematics and instrumental broadening. For a given set of model parameters (θ), the model spectrum is then compared with the dust-corrected spectrum to calculate a χ^2 -like likelihood:

$$\ln L(\theta) \propto -\frac{1}{2} \sum_{i,j=1}^N (f_{\theta,i} - f_{D,i}) (\mathcal{M}^{-1})_{ij} (f_{\theta,j} - f_{D,j}) \quad (4)$$

where $f_{\theta,i}$ is the predicted flux at the i -th wavelength pixel given the parameter set θ , $f_{D,i}$ is the flux of the dust-corrected spectrum at the same wavelength, and N is the total number of wavelength pixels. The covariance matrix of the data, $\mathcal{M}_{ij} \equiv \langle \delta f_{D,i} \delta f_{D,j} \rangle$, is assumed to be diagonal and specified by the error spectrum. With a flat prior and the above likelihood function, BIGS utilizes the MULTINEST sampler (Feroz et al. 2009, 2013) through a PYTHON interface (Buchner et al. 2014) to sample the posterior distributions of all the model parameters, which are stored and used for subsequent analysis.

The best-fit model spectrum obtained for the example spaxel from the posterior distributions of the model parameters is plotted in yellow in the middle panel of Figure 1. In the rightmost panel of the same figure, the observed and the best-fit model spectra are plotted again, but over a wider range of wavelength. As can be seen, the model spectrum covers not only the optical range, but also extends to both NUV and NIR. Note, however, that the technique of Li et al. (2020)

yields dust attenuation curves that are relative. Thus, both the dust-corrected spectrum and the best-fit model spectrum are also relative, with arbitrary amplitudes to be determined. Assuming that dust attenuation is negligible in NIR, we can obtain the absolute normalization of the model spectrum by matching the Ks-band magnitude of the spaxel in the 2MASS image with the model magnitude in the same band. This normalization scheme is used in Figure 1 and in our following analysis.

3.2. Characterizing the dust attenuation and the 2175Å bump

Given the flux-calibrated dust-free model spectrum derived above, one can obtain the unattenuated magnitude for a specific band by convolving the model spectrum with the corresponding filter response function, and thus the absolute attenuation in the band by comparing the observed magnitude with the unattenuated magnitude. Here, we consider five bands: B and V in the optical and the three *Swift*/UVOT bands (uvw2, uvm2 and uvw1). Following common practice and for each spaxel with spectral $S/N > 20$, we have estimated the following quantities to characterize the dust attenuation in both optical and NUV:

- A_B, A_V — stellar dust attenuation in B and V band.
- $E(B-V) \equiv A_B - A_V$ — color excess in the optical.
- $R_V \equiv A_V/E(B-V)$ — total-to-selective attenuation ratio in V band. This parameter has been commonly used to characterize the slope of attenuation curves. For example, $R_V = 4.05$ for a standard Calzetti curve, and $R_V = 3.1$ for a Milky Way-like curve (e.g. Cardelli et al. 1989).
- A_B/A_V — optical slope of the attenuation curve defined following Salim & Narayanan (2020). We have $A_B/A_V = 1.25$ and 1.32 for the Calzetti and Milky Way curves, respectively.
- A_{w2}, A_{m2}, A_{w1} — stellar dust attenuation in NUV bands.
- A_{w2}/A_{w1} — NUV slope of the attenuation curve, which is similar to, but not exactly the same as the definition in Salim & Narayanan (2020) where the UV slope is defined as the ratio of extinctions at 1000Å and 3000Å. With our definition, we have $A_{w2}/A_{w1} = 1.19$ for the Calzetti attenuation curve and $A_{w2}/A_{w1} = 1.24$ for the Milky Way curve.

In the rightmost panel of Figure 1, the observed SED of the example spaxel is plotted as red stars, and the

stellar attenuation parameters, A_V , A_{w2} , A_{m2} and A_{w1} , are indicated by the vertical dashed lines.

Next, we estimate two more parameters to characterize the 2175Å bump. The first parameter is A_{bump} , defined as

$$A_{\text{bump}} \equiv A(2175\text{\AA}) - A'(2175\text{\AA}), \quad (5)$$

where $A(2175\text{\AA})$ is the total attenuation at 2175Å and $A'(2175\text{\AA})$ is the attenuation at the same wavelength in the absence of a 2175Å bump. Thus, A_{bump} is a measure of the *extra* attenuation around 2175Å relative to that without a 2175Å bump. Considering that the central wavelength of the uvm2 band (2246Å) is close to 2175Å, we simply use A_{m2} derived above to approximate $A(2175\text{\AA})$ in the definition. The equation can thus be rewritten as

$$\begin{aligned} A_{\text{bump}} &= A_{m2} - A'_{m2} \\ &= (\text{uvm2} - \text{uvm2}_0) - (\text{uvm2}' - \text{uvm2}_0) \\ &= \text{uvm2} - \text{uvm2}', \end{aligned} \quad (6)$$

where all the quantities are defined in the uvm2 band, and a prime denotes the absence of a 2175Å bump. The observed magnitude uvm2 and the unattenuated magnitude uvm2₀ can be readily measured from the observed and the dust-free model spectrum. However, the expected magnitude in the absence of the 2175Å bump, uvm2', cannot be obtained in a straightforward way. We follow the generally-adopted assumption that, in the absence of the 2175Å bump, the UV stellar continuum can be well described by a power-law of $F(\lambda) \propto \lambda^{-\beta}$ (e.g. Calzetti et al. 1994; Battisti et al. 2016). With this assumption, we can use fluxes in uvw1 and uvw2, both located far away from 2175Å, to determine a power-law continuum in NUV, which is then used to estimate uvm2'. The power-law continuum and A_{bump} derived this way are indicated in the right panel of Figure 1 for the example spaxel.

The second parameter is the bump strength, B , defined as follows following common practice:

$$B \equiv A_{\text{bump}}/A'_{m2} = A_{\text{bump}}/(A_{m2} - A_{\text{bump}}). \quad (7)$$

So defined, $B = 0.19$ for a Milky Way-type dust curve, and $B = 0$ for a Calzetti curve (no bump). As the bump strength parameter is defined relative to A'_{m2} , the uncertainty becomes large when A'_{m2} is close to zero. Previous investigations generally exclude sample objects with low total attenuation to avoid this problem. For instance, Kriek & Conroy (2013) only used galaxies with $A_V > 0.2$ for their study. Here we adopt a lower limit of $A_V = 0.25$ and exclude all spaxels with A_V below this limit. Together with the requirement of $S/N > 20$, this

restriction gives a sample of 1018 spaxels, which are distributed in 71 galaxies and are used for the analysis in the next section.

3.3. Global measurements

For comparison with previous studies, which are mostly limited to global measurements, we stack all the spaxels within $1 R_e$ to generate an integrated spectrum for each of the 134 galaxies in the SwiM catalog, following the procedure described in Zhou et al. (2020). The *Swift*/UVOT images and 2MASS Ks-band image are also co-added correspondingly to derive the photometry within $1 R_e$ for each galaxy. We are left with a sample of 72 galaxies after applying the same selection criteria: $\text{SNR} > 20$, and $A_V > 0.25$. Note that the 71 galaxies where the 1018 spaxels come from are all in this sample, with one additional galaxy included due to the increase of SNR during the stacking. We apply the same method as described above to perform spectral fitting for each galaxy and to measure the global dust attenuation properties defined in the same way as above.

3.4. Tests on mock spectra

In order to test our method, we have generated a set of mock spectra that cover a variety of dust attenuation properties and spectral SNRs. We first obtain various SFHs using the $\Gamma+B$ model described in Section 3 with randomly generated model parameters. These SFHs are combined with the BC03 SSP model spectra assuming a Chabrier IMF to generate composite spectra covering a wide range in stellar population properties. Random noise following Gaussian distributions of different widths is added to the spectra to produce SNRs ranging from 10 to 70. To include dust attenuation with different dust opacity, curve slopes and 2175Å bump strengths, we use the functional form proposed by Conroy et al. (2010) (see equations A1-A12 in the paper, hereafter the CSB curve). This flexible curve allows variations in A_V , slopes characterised by R_V , and the 2175Å bump strength characterised by the parameter B_{CSB} (with $B_{\text{CSB}} = 1.0$ being the bump strength of the Milky-Way curve). We randomly generate attenuation curves with $0 < A_V < 3$, $1 < R_V < 10$ and $0 < B_{\text{CSB}} < 1.5$, and apply them to the mock spectra. The dust-attenuated spectra are then convolved with the filter response functions of 2MASS Ks and the three *Swift*/UVOT bands to calculate the magnitudes. We add Gaussian noise with a standard deviation of $\sigma_{Ks} = 0.07$ to the Ks band and of $\sigma_{UV} = 0.13$ to uvw2, uvm2 and uvw1 bands. These values correspond to the typical uncertainties in the real data. Repeating this process, we generated a sample of 1000 mock spectra/SEDs of different SNRs, with known stellar populations and dust attenuation properties.

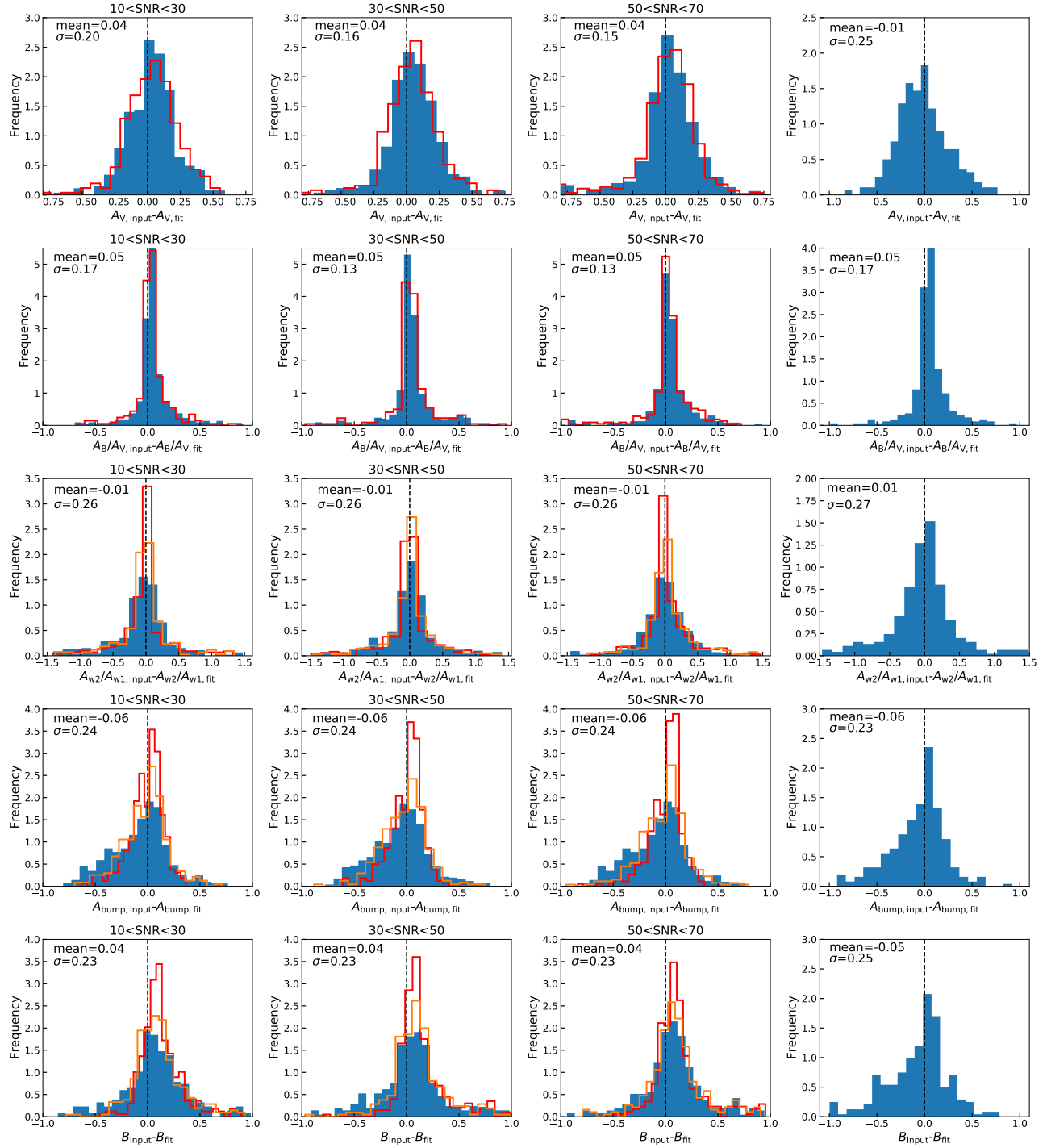


Figure 2. Results of the test of our method on mock spectra. The histograms show the distributions of the difference between the input and the estimated values for five dust parameters (panels from top to bottom): A_V , A_B/A_V , A_{w2}/A_{w1} , A_{bump} and B . In each row, the left three panels show the results for three SNR ranges (as indicated) as obtained with the BC03 stellar templates, while the rightmost panel shows the result with the BPASS stellar templates for the SNR range of 10 < SNR < 30. In each panel, the filled blue histogram shows the result from mock spectra that include Gaussian noise with a standard deviation of $\sigma_{K_s} = 0.07$ in the Ks band and $\sigma_{UV} = 0.13$ in the uvw2 and uvw1 bands, with the mean and standard deviation of the distribution indicated at the top-left corner. Red histograms in the top two rows are results obtained by assuming a smaller uncertainty in the Ks band with $\sigma_{K_s} = 0.02$, while the orange and red histograms in the lower three rows show results obtained with smaller uncertainties in NUV bands, with $\sigma_{UV} = 0.05$ (orange) and $\sigma_{UV} = 0.02$ (red). All histograms are normalized to have a total of unity. Overall, the test results show that our method adequately recovers the input properties of dust attenuation with systematic and statistical errors well under control.

We apply our method to the mock data to estimate the same parameters as described above and compare them with the input parameters. Figure 2 (the left three columns) shows the results for five parameters: A_V , A_B/A_V , A_{w2}/A_{w1} , A_{bump} and B . Panels from top to bottom correspond to the five parameters, and panels from left to right correspond to three ranges of SNRs: $10 < \text{SNR} < 30$, $30 < \text{SNR} < 50$, $50 < \text{SNR} < 70$, respectively. In each panel the filled histogram plotted in blue shows the distribution of the 1000 mock spectra in the difference between the input and output parameters. It is encouraging that, overall, all the four parameters are well recovered with only weak or no bias. For the dust parameters in the optical, i.e. A_V and A_B/A_V , the standard deviation σ decreases significantly as one goes from the first SNR bin, where $\sigma(A_V) = 0.20$ and $\sigma(A_B/A_V) = 0.17$, to the second SNR bin, where $\sigma(A_V) = 0.16$ and $\sigma(A_B/A_V) = 0.13$, with no further decrease as the SNR exceeds 30. For the parameters in the UV, i.e. A_{w2}/A_{w1} , A_{bump} and B , the standard deviation does not depend on SNR, with $\sigma(A_{w2}/A_{w1}) = 0.26$, $\sigma(A_{\text{bump}}) = 0.24$ and $\sigma(B) = 0.23$ at all SNRs.

Using mock spectra generated in a similar way, Li et al. (2020) found that their method can reproduce $E(B - V)$ without bias but with a standard derivation of $\sigma \sim 0.022 - 0.05$ mag at $10 < \text{SNR} < 30$ (see their Fig.7), corresponding to $\sim 0.1 - 0.2$ mag in A_V assuming a Calzetti curve with $R_V = 4.05$. For the same SNR range we find a similar but slightly larger standard deviation with $\sigma(A_V) = 0.20$ mag, implying that the uncertainties in the dust parameters are not purely limited to the spectral SNR. The uncertainty in the Ks-band photometry could be one of the factors. We have repeated the same test but adopting a smaller uncertainty in the Ks-band magnitude: $\sigma_{Ks} = 0.02$, and we show the result as red histograms in the upper two rows in Figure 2. The results are similar to the filled blue histograms obtained with $\sigma_{Ks} = 0.07$, suggesting that the NIR photometry is not a dominating source of uncertainty in the estimated dust parameters. Similarly, we have done tests using mock data with smaller uncertainties in the UV photometry, $\sigma_{UV} = 0.05$ and 0.02 for the three *Swift*/UVOT bands. The predicted distributions, plotted as orange and red histograms in the lower three rows in Figure 2, appear to be significantly narrower than the corresponding filled blue histograms. Together with the weak dependence on SNR, this indicates that the uncertainties in A_{w2}/A_{w1} , A_{bump} and B are dominated by the *Swift*/UVOT photometry.

The results presented above are based on the stellar population model of BC03. Although this model has been widely used, different stellar population templates

(e.g. Maraston 2005; Vazdekis et al. 2010; Eldridge et al. 2017) may lead to different results, particularly in NIR and UV. To fully account for the systematics introduced by different SSP templates is beyond the scope of this work. Here we present a simple test to examine the impacts of this issue. In this test, we apply the same method to the same set of mock spectra generated from BC03 SSP templates, but the SSP models from the Binary Population and Spectral Synthesis (BPASS; Eldridge et al. 2017) instead of the BC03 models are used in the fitting process. Compared to the BC03 models, the BPASS templates take into account the evolution of binaries, and thus are different in many aspects, especially in the UV range. The results of this test are shown in the rightmost column in Figure 2, but only for the lowest S/N range ($10 < \text{SNR} < 30$) for simplicity. Comparing the results with the blue filled histograms shown in the leftmost column, we see that the standard deviation of A_V increases slightly from 0.2 to 0.25 mag, but that all the five parameters are recovered with similarly weak bias and small standard deviations. These results indicate that the uncertainties in dust slopes and bump strengths are mostly dominated by uncertainties in flux measurements and the method itself, and that using different SSP templates should not significantly affect our main results.

In the tests above, the uncertainties in the spectra and SEDs are modeled to some degree by including a component of Gaussian noise. However, real observational uncertainties may be more complicated. For example, uncertainties in flux calibration and in sky contamination may not be characterised by a simple Gaussian noise and may lead to systematic bias. In addition, it is possible that a small population of young or intermediate-age stars in the galaxy that do not affect the optical spectrum very much may contribute to the light in NUV. In this case the difference between the best-fit and observed *uvw2*, *uvm2* and *uvw1* fluxes will not give an accurate estimate of A_{w2} , A_{m2} , A_{w1} . However, the $\Gamma+B$ model used in our mock test has naturally allowed the presence of an arbitrary fraction of stars of different ages and metallicities. The similarity of the overall scatter as seen in the mock and real spectral fitting (see results in section 4) indicates that these effects are not significant and the main uncertainties should have been captured in our method.

Based on the tests we conclude that, as long as the spectral SNR is sufficiently high (e.g. $\text{SNR} > 10$ considered in the test), the NIR photometry is not the main source of uncertainties. The uncertainties in the dust parameters in UV may be further reduced by increasing the quality of the UV photometry. Given the quality of the

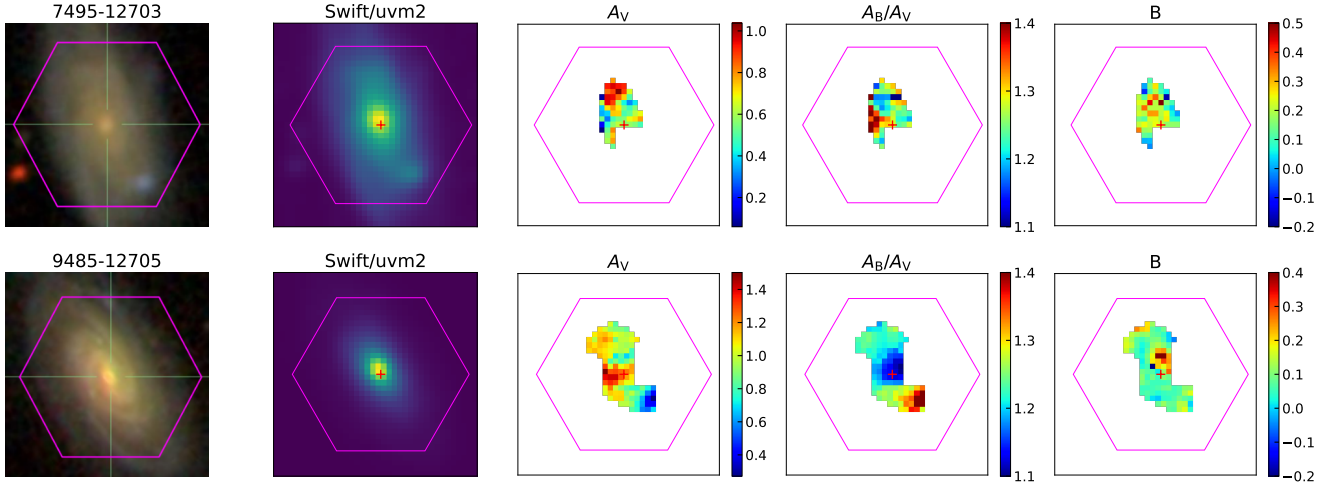


Figure 3. Two example galaxies in our sample. From left to right, plots show the optical image, Swift *uvm2* image, the absolute attenuation in V band (A_V), the slope of the attenuation curve in optical (A_B/A_V), and the bump strength B in each galaxy. In each panel, the MaNGA footprint is shown in magenta, with a red cross marking the center of the integral field.

real data used in our study, $\text{SNR} > 20$, $\sigma_{K_s} \sim 0.07$ and $\sigma_{UV} \sim 0.13$, our method is expected to recover the average properties of dust attenuation in individual spaxels with systematic and statistical errors well under control.

4. RESULTS

We obtained the dust properties in our sample galaxies using the method presented above. Before digging into detailed statistical results for the dust parameters, we show in [Figure 3](#) two example galaxies that have a large number of spaxels satisfying our selection criteria. As seen from the plot, the dust properties, including the absolute attenuation in V band (A_V), the slope of the attenuation curve in optical (A_B/A_V), and the 2175Å bump strength B , vary significantly across the galaxy, which signifies the importance of spatially resolve data such as MaNGA and Swift/UVOT in investigating the dust properties in galaxies. It is also noticeable that these dust properties are not randomly distributed in the galaxy, but rather some correlations are seen between the parameters. In what follows we will use the entire sample to examine the variation of the different dust properties, as well as the correlations between the dust properties.

4.1. Amplitudes and slopes of the attenuation curves

We first examine the amplitude and slope of the dust attenuation curve and their dependence on star formation rate and stellar mass. To this end, we take the measurements of $\text{H}\alpha$ emission line flux provided by the MaNGA DAP for all the spaxels in our sample, and estimate a star formation rate (SFR) for each spaxel from the $\text{H}\alpha$ luminosity by $\text{SFR}(\text{M}_\odot\text{yr}^{-1}) = 7.9 \times 10^{-42} L(\text{H}\alpha)$ (Kennicutt 1998). Stellar masses for

individual spaxels are obtained from the MaNGA spectra as a byproduct of the technique of Li et al. (2020) described in § 3.1. We have also obtained the global measurements of the SFR for the 72 galaxies by adding up SFRs for all individual spaxels in each galaxy, while the total stellar masses of these galaxies are taken from the NSA.

In [Figure 4](#) we examine the correlations of the absolute attenuation in the V band (A_V) with the specific star formation rate (sSFR) on a logarithmic scale, $\log_{10}(\text{sSFR}) \equiv \log_{10}(\text{SFR}/M_*)$. In both panels, the solid black line displays the median of all the spaxels, while the gray and light gray regions indicate the 1σ and 2σ scatter of individual spaxels around the median. The global measurements of the 72 galaxies are plotted as colored stars, color-coded by their total stellar mass. As can be seen, our samples of both individual spaxels and the global measurements span a wide range in both A_V and $\log_{10}(\text{sSFR})$. The global measurements present a similar distribution to the spaxels, and the distribution does not depend significantly on the total stellar mass of galaxies. The median A_V of spaxels increases from $A_V \sim 0.3$ mag at the lowest sSFR to $A_V \sim 0.8$ mag at $\log_{10}(\text{sSFR}/\text{Gyr}^{-1}) \sim -1.8$, remaining roughly at a constant level at higher sSFRs. This is consistent with that obtained by Li et al. (2021) who found a similar trend of the stellar color excess $E(B - V)$ of kpc-sized regions with sSFR (see figure 14 in that paper). The scatter among spaxels at a given sSFR is $\sigma \sim 0.4$ mag, and shows a slightly positive correlation with sSFR. Assuming an average scatter of $\lesssim 0.2$ mag expected to be caused by the uncertainties in our method and data (see § 3.4) and a total scatter of ~ 0.4 mag as shown in the

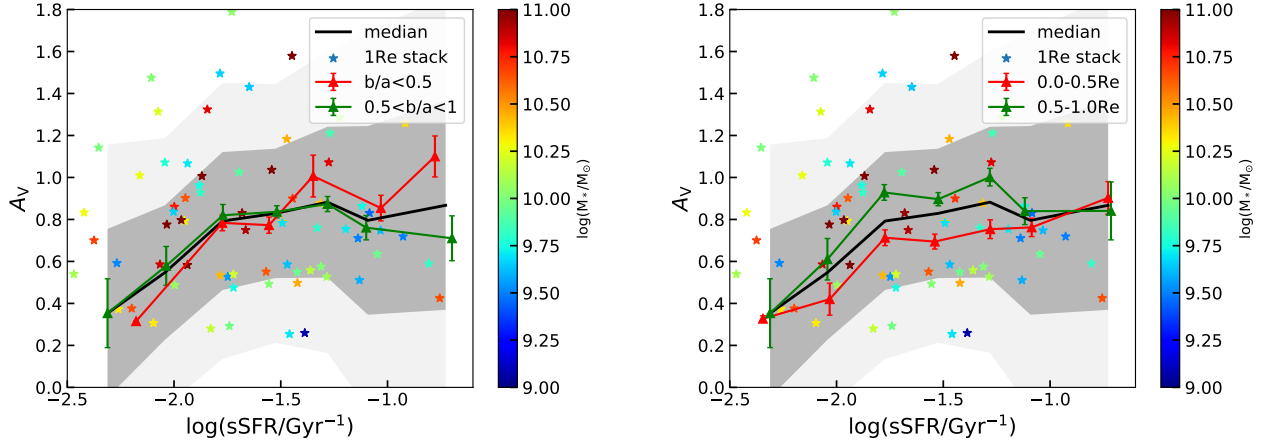


Figure 4. *Left:* The absolute attenuation in V band (A_V) as a function of the sSFR. The black line shows the median relation of all the pixels in our galaxies, and the grey and light-grey shaded regions indicate the 1σ and 2σ scatter of individual spaxels around the median. Stars are the results from the stacked spectra within $1R_e$ of each galaxy, color-coded by the total stellar mass of the galaxy indicated by the color bar. The red/green triangles/lines show the results for subsamples of spaxels selected by b/a , the minor-to-major axis ratio of the SDSS r -band image of the host galaxies. *Right:* Same as left, except that the red/green triangles/lines are for subsamples selected by the galactocentric distance of the spaxels.

figure, we estimate that on average the intrinsic scatter is $\sigma \gtrsim 0.35$ mag for our sample.

We have attempted to examine the potential sources responsible for the intrinsic scatter in the A_V -sSFR relation by dividing the spaxels of given sSFR into two subsamples according to either the minor-to-major axis ratio (b/a) of the SDSS r -band image of the host galaxy or the galactocentric distance of the spaxels scaled by the effective radius (R_e) of the galaxy. The results of the subsamples selected by b/a are plotted in the left panel of Figure 4 as red/green triangles connected by red/green lines. We find no dependence on b/a , indicating that galaxy inclination (geometry of dust distribution) does not explain the observed scatter. The results of the subsamples selected by the galactocentric distance of spaxels are shown in the right panel of the same figure. For comparison, the results of the full samples of both spaxels and galaxies shown in the left panel are repeated here. A weak but significant dependence on the galactocentric distance is seen at intermediate sSFRs, where spaxels within $0.5R_e$ tend to have smaller A_V at fixed sSFR than spaxels located between $0.5R_e$ and R_e . However, the difference in A_V is at a level of 0.2 mag at most between the two subsamples, implying that the location of spaxels cannot fully account for the overall scatter. The residual dependence on the location of spaxels indicates some variation of dust attenuation between the central bulge and the outer disk, but more work is needed to better understand the variation.

Next, we examine the correlation of the attenuation curve slope in optical (A_B/A_V) with the sSFR, and the

results are shown in Figure 5. The median of and scatter among spaxels are plotted as the black solid line and shaded region, respectively, and the global measurements are plotted as colored stars. In panels from left to right, colored triangles/lines show results of subsamples of spaxels selected by A_V (left), b/a (middle) and the galactocentric distance (right), respectively. In each panel, the blue dashed line indicates the Calzetti curve, which has $A_B/A_V = 1.25$, while the red dashed line indicates the Milky Way-type curve with $A_B/A_V = 1.32$. The Milky Way itself is plotted as a big blue dot in each panel. Overall, A_B/A_V presents a median value that is roughly constant at all sSFRs and is very close to the slope of the Calzetti curve, with a 1σ scatter of $\sigma(A_B/A_V) \sim 0.15$ quite independent of the sSFR. The Milky Way-type curve falls within the 1σ range.

In Figure 6 we further examine the correlation of the slope in UV (A_{w2}/A_{w1}) with sSFR. Symbols/lines/colors are coded in the same way as in the previous figure. We find that A_{w2}/A_{w1} appears to have an anti-correlation with sSFR, but the correlation is quite weak given the large scatter among the spaxels. The median value of A_{w2}/A_{w1} is closer to the Milky-Way type at low sSFR and closer to the Calzetti curve at high sSFR, despite the small difference between the two model curves. This indicates the flattening of the NUV attenuation curve in star-forming regions.

In both Figure 5 and Figure 6 we do not observe any clear trends with the total stellar mass of galaxies. It is interesting to note that the 1σ scatter in both figures, $\sigma \sim 0.15$ for A_B/A_V and $\sigma \sim 0.25$ for A_{w2}/A_{w1} , is

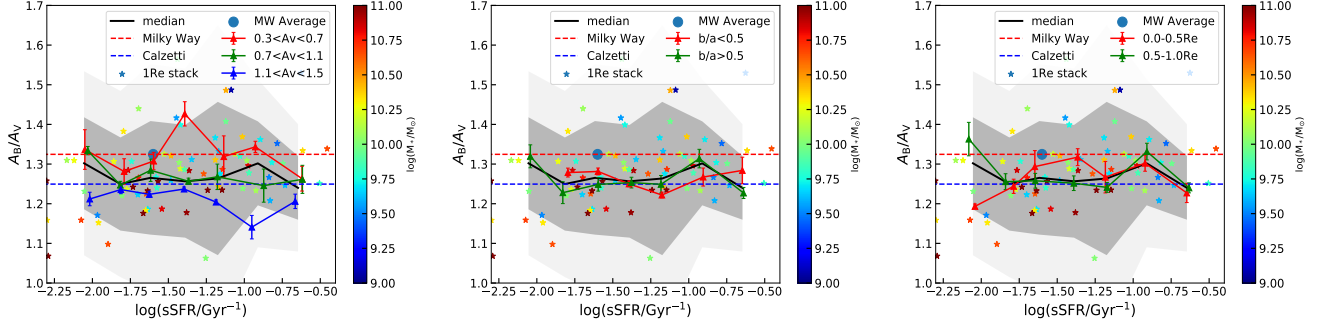


Figure 5. The slope of the attenuation curve in optical (A_B/A_V) as a function of the sSFR. The black line shows the median values of the results obtained from individual pixels, with grey shaded regions indicates 1σ and 2σ scatters of the data points. Stars are results from the 1Re stacks of each galaxy, with color codes showing the total stellar mass of the galaxy (from NSA). In panels from left to right, colored triangles/lines show results of subsamples of spaxels selected by A_V (left), b/a (middle) and the galactocentric distance (right), respectively.

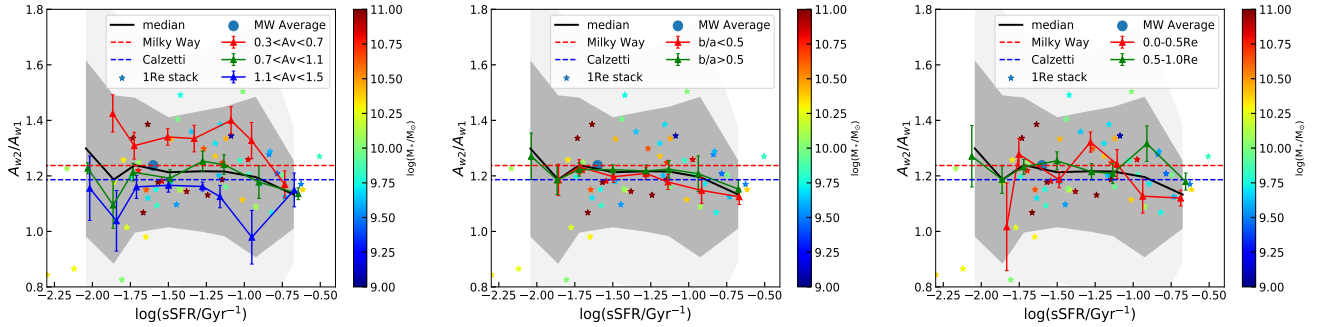


Figure 6. The slope of the attenuation curve in NUV (A_{w2}/A_{w1}). The black line shows the median values of the results obtained from individual pixels, with grey shaded regions indicates 1σ and 2σ scatters of the data points. Stars are results from the 1Re stacks of each galaxy, with color codes showing the total stellar mass of the galaxy (from NSA). In panels from left to right, colored triangles/lines show results of subsamples of spaxels selected by A_V (left), b/a (middle) and the galactocentric distance (right), respectively.

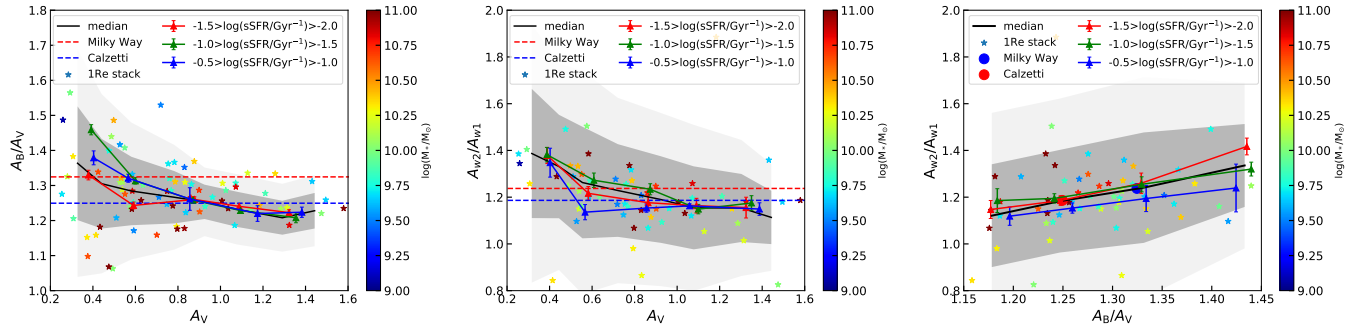


Figure 7. The mutual relation between the dust opacity in V-band (A_V) and the slopes of the attenuation curve in optical (A_B/A_V , left) and NUV (A_{w2}/A_{w1} , middle), with the mutual relation between A_B/A_V and A_{w2}/A_{w1} showing in the right panel. The black line shows the median values of the results obtained from individual pixels, with grey shaded regions indicates 1σ and 2σ scatters of the data points. Stars are results from the 1Re stacks of each galaxy, with color codes showing the total stellar mass of the galaxy (from NSA). In the left and middle panels the slopes for the Milky Way curve and Calzetti curve are indicated as blue and red dash lines, while in the right panel they are marked as blue and red dots respectively.

comparable to the scatter predicted by the test in § 3.4, $\sigma \lesssim 0.17$ and $\sigma = 0.26$ for the two parameters, respectively. This indicates that the intrinsic scatter in both A_B/A_V and A_{w2}/A_{w1} is small once the sSFR is limited to a narrow range. When dividing spaxels into subsamples, we find no significant dependence of the slope-sSFR relation on b/a and the galactocentric distance, suggesting that the inclination of the host galaxy and the location within the host are not the reasons for the scatter. In contrast, at fixed sSFR the slopes in both optical and NUV show significant and systematic trends with A_V . This effect is more pronounced in NUV where the dependence on A_V is similarly seen for all sSFRs except at the highest end. For the optical slope, the A_V dependence is mainly seen in the intermediate range of sSFR.

To see the A_V dependence of the slope more clearly, in Figure 7 we plot A_B/A_V (left panel) and A_{w2}/A_{w1} (middle panel) as functions of A_V , as well as the relation between A_B/A_V and A_{w2}/A_{w1} themselves (right panel). Results for three subsamples selected by \log_{10} sSFR are plotted as colored triangles connected by lines. On average the slopes in both optical and NUV are anti-correlated with A_V . In both the optical and NUV bands, a Calzetti slope is preferred by spaxels/galaxies with $A_V \sim 0.9$ mag. The slope becomes comparable to or steeper than the Milky-Way type at lower A_V , and flatter than the Calzetti curve at higher A_V . At $A_V \gtrsim 0.8$, the slope- A_V relation remain similar even when spaxels are divided into narrow ranges of sSFR, suggesting that the slope is primarily determined by A_V rather than by sSFR in regions of high dust opacity. At $A_V \lesssim 0.8$, the anti-correlations between the slope and A_V may be partly attributed to the positive correlation between A_V and sSFR at the low ends of opacity and sSFR (see Figure 4). Also note that at the low ends of A_V the scatters of the correlation are significantly larger than at the higher end, especially in the left panel. This is expected as the uncertainty of A_B/A_V directly correlates with the absolute value of A_V and the results again signify the importance of excluding spaxels of very low A_V in our analysis. Our results confirm that a Calzetti curve is valid for star-forming galaxies with large dust contents, while dust curves of steeper slopes may be needed for galaxies with low optical opacity.

The right panel of Figure 7 shows that the two slopes are positively and (almost) linearly correlated with each other, with scatter that is comparable to that seen in the test (§ 3.4). Both the Milky Way and Calzetti curves lie on the median relation of our sample, but the variance among individual galaxies is large. This again suggests that dust attenuation laws in galaxies cannot be fully characterized by curves with a single slope. These re-

sults are consistent with those obtained previously (e.g. Salim et al. 2018), and with radiative transfer model predictions taking into account complex dust-gas distributions (Narayanan et al. 2018). Since previous observations have been mostly limited to global relations of galaxies, our results show for the first time that these correlations also hold for regions of kpc scales within individual galaxies. As can be seen, the median relations remain almost unchanged when the sSFR is limited to narrow ranges, consistent with the weak dependence of the slope on sSFR seen in Figure 5 and Figure 6.

4.2. The 2175Å bump

In Figure 8, we plot the attenuation excess due to the 2175Å bump (A_{bump} , top) and normalized bump strength (B , bottom), estimated for spaxels and galaxies as a function of $\log_{10}(\text{sSFR})$. The results for spaxels as a whole and for individual galaxies are plotted with the same symbols/lines coding as in the previous figures, and are repeated in the three panels that show results for subsamples selected by A_V (left), b/a (middle) and galactocentric distance (right). The values of B obtained from our samples range from ~ 0 to ~ 0.5 , broadly consistent with the strengths reported for galaxies at high redshift ($1 < z < 2$, Buat et al. 2011; $0.5 < z < 2$, Kriek & Conroy 2013; $z \sim 2$, Shivaei et al. 2022). Both A_{bump} and B decrease with increasing sSFR, with a median bump strength that is comparable to or stronger than that of the Milky Way-type bump in quiescent regions with $\log_{10}(\text{sSFR}/\text{Gyr}^{-1}) \lesssim -1.8$, and consistent with the Calzetti curve with $B = 0$ in star-forming regions with the highest sSFRs. This result is also consistent with previous findings based on global measurements of high- z galaxies (e.g. Kriek & Conroy 2013; Kashino et al. 2021), as well as with the absence of the 2175 Å bump in local starburst galaxies used to derive the Calzetti curve (Calzetti et al. 1994, 2000).

From Figure 8 and for both the A_{bump} -sSFR relation and the B -sSFR relation, we find no obvious dependence on A_V , b/a and the galactocentric distance in all the panels except the top-left panel where the spaxels with $A_V < 0.6$ and $\log_{10}(\text{sSFR}/\text{Gyr}^{-1}) \gtrsim -1.7$ appear to have smaller A_{bump} at fixed sSFR than those with higher optical opacities. This result indicates that the properties responsible for the variation of the 2175Å bump in galaxies are not sensitive to the total attenuation, global inclination of galaxies and the location within individual galaxies. Instead, the variation may be related to processes on scales smaller than the sizes of individual spaxels (kpc scales) studied here.

In Figure 9, we further examine A_{bump} (upper panels) and B (lower panels) as a function of A_V (left panels),

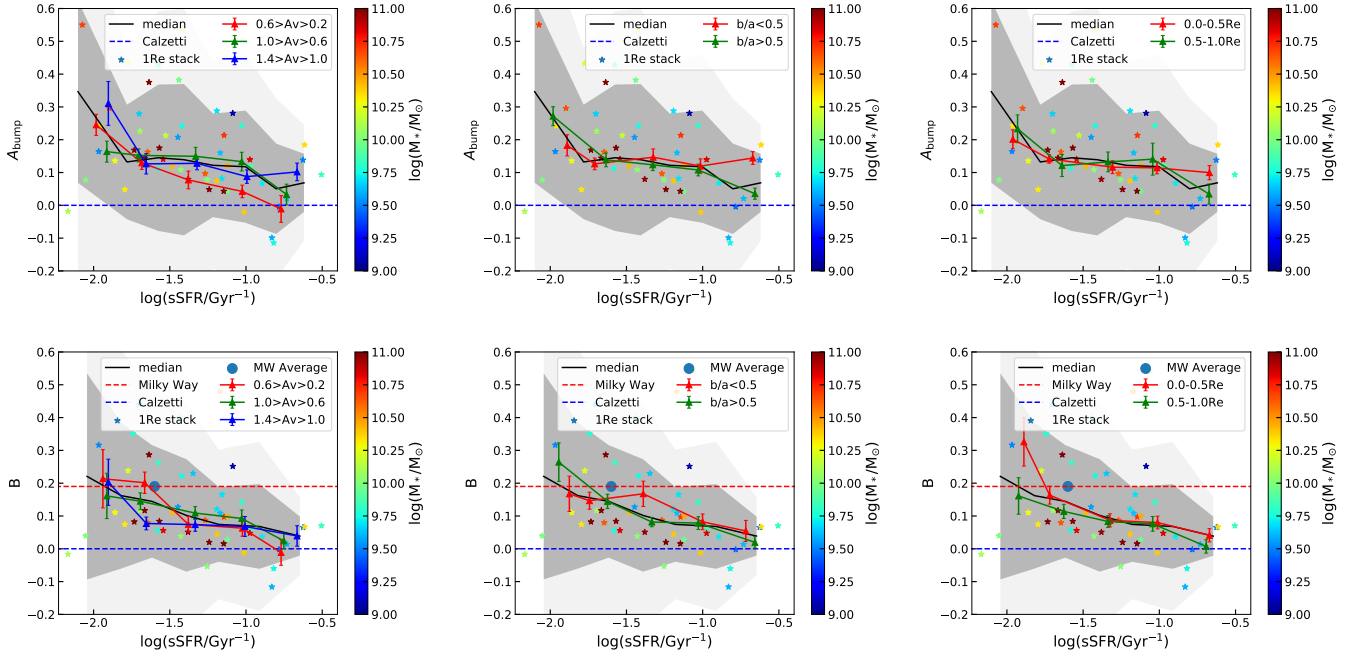


Figure 8. The attenuation excess due to the 2175Å bump (A_{bump} , top) and normalized bump strength (B , bottom) in our sample as a function of sSFR. The black line shows the median values of the results obtained from individual pixels, with grey shaded regions indicates 1σ and 2σ scatters of the data points. Stars are results from the 1Re stacks of each galaxy, with color codes showing the total stellar mass of the galaxy (from NSA). In panels from left to right, colored triangles/lines show results of subsamples of spaxels selected by A_V (left), b/a (middle) and the galactocentric distance (right), respectively. In bottom panels, the bump strength for the Milky-Way and Calzetti dust curve are indicated as red and blue dash lines respectively, with a blue circle indicating the average value of the Milky Way ($\log(\text{sSFR}/\text{Gyr}^{-1}) \sim -1.6$).

A_B/A_V (middle panels), and A_{w2}/A_{w1} (right panels). As in previous figures, in each panel the black line and the shaded regions present the median relation and the 1σ and 2σ scatter of individual spaxels around the median, while the colored triangles connected by the solid lines display the results for subsamples selected by sSFR. The red and blue dashed lines in the left panels indicate the relations for the Milky Way-like and Calzetti attenuation curves. If the attenuation curve has a fixed Milky Way-like shape, one would expect a fixed bump strength ($B = 0.19$) and a linearly increasing A_{bump} with increasing A_V . This correlation is not seen in our result, however. As can be seen from the upper-left panel, A_{bump} at scales of both spaxels and galaxies shows no significant correlation with A_V and this result is held at limited ranges of sSFR. In the lower-left panel the median B parameter of all the spaxels tends to present a marginal anti-correlation with A_V , which becomes rather insignificant when the spaxels are divided into sSFR intervals. In the middle and right panels, A_{bump} and B show no obvious correlation with the attenuation curve slope in both optical and NUV bands, which is similar to the results reported by Barišić et al. (2020) based on spectroscopy of galaxies at $z \sim 0.8$ from the LEGA-C survey.

Figure 9 also shows that the overall scatter of the bump properties at fixed A_B/A_V or A_{w2}/A_{w1} can be largely explained by the correlation of the bump parameters with sSFR as seen in Figure 8. Combined with the null correlation of the bump properties with the attenuation curve parameters, this result indicates that the variation of the 2175Å bump and the variation of the attenuation curve are unlikely to be driven by the same process. It is likely that the variation of the 2175Å bump strength is driven by star formation-related processes, such as the destruction of the bump carriers by the UV radiation produced by newly formed massive stars (e.g. Fischera & Dopita 2011). We will come back and discuss this point in the next section.

5. DISCUSSION

5.1. Methods of deriving dust attenuation curves

In order to derive the attenuation curve for a galaxy or a resolved region, one has to obtain the intrinsic, dust-free spectrum or SED in the first place. In previous studies this was done usually in two different ways, either by empirically comparing observed SEDs/spectra between dusty galaxies and those with no or relatively weak attenuation (e.g. Calzetti et al. 1994; Kinney et al.

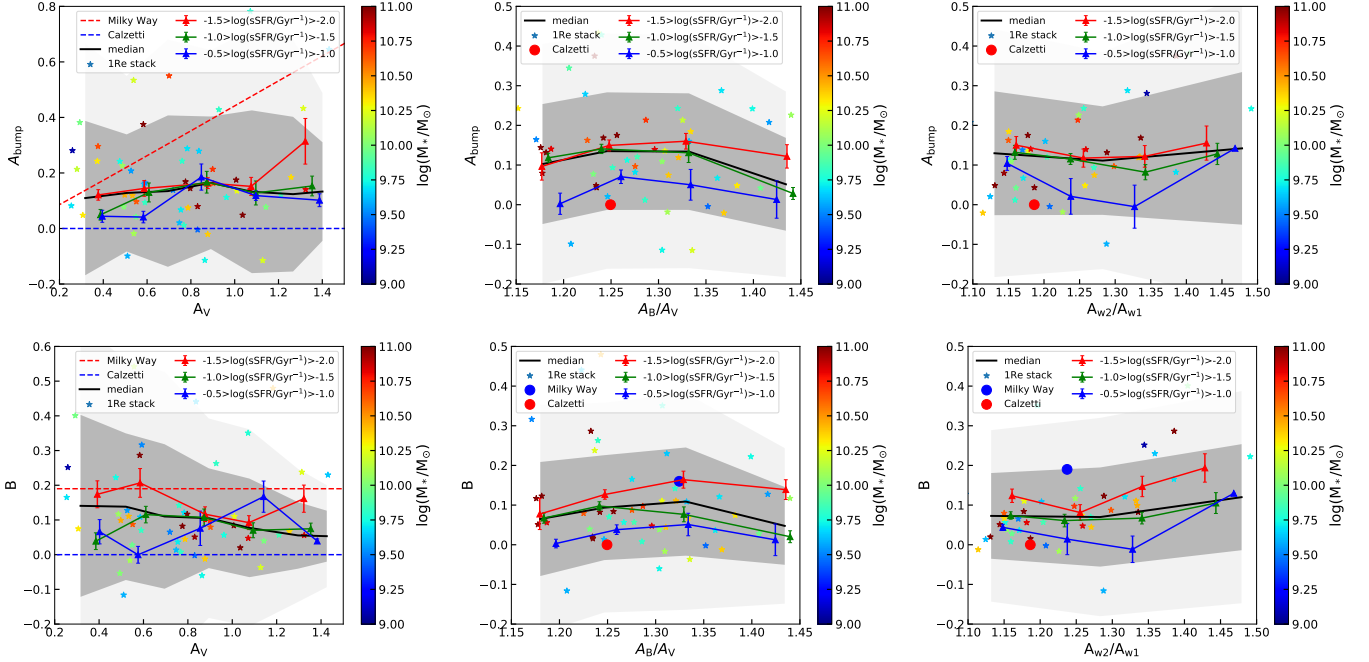


Figure 9. The attenuation caused by the 2175Å bump (A_{bump} , top) and normalized bump strength (B , bottom) in our sample as a function of A_V (left) and the slopes of the attenuation curve in optical (A_B/A_V , middle) and NUV (A_{W2}/A_{W1} , right). The black line shows the median values of the results obtained from individual pixels, with grey shaded regions indicating 1σ and 2σ scatters of the data points. Stars are results from the 1Re stacks of each galaxy, with color codes showing the total stellar mass of the galaxy (from NSA). In panels from left to right, colored triangles/lines show results of subsamples of spaxels selected by A_V (left), b/a (middle) and the galactocentric distance (right), respectively. Values for the Milky-Way and Calzetti dust curve are indicated in red and blue respectively.

1994; Calzetti 1997; Calzetti et al. 2000; Johnson et al. 2007; Wild et al. 2011; Battisti et al. 2016, 2017), or based on stellar population synthesis (SPS) models (e.g. Spinrad & Taylor 1971; Faber 1972; Sawicki & Yee 1998; Papovich et al. 2001; Kauffmann et al. 2003; Salim et al. 2005, 2007; Noll et al. 2009a; Conroy 2013; Leja et al. 2017; Boquien et al. 2019; Johnson et al. 2019; Zhou et al. 2019; Boquien et al. 2022; Jones et al. 2022; Nagaraj et al. 2022).

As pointed out by Wild et al. (2011), in the empirical method the template or the galaxy in a pair with higher attenuation will contribute more to the final average curve if the curve slope depends on the dust attenuation itself, as is observed in previous studies and in Figure 7. Since the dust content varies across a galaxy and the dust curve slopes span a wide range, as revealed by our spatially resolved measurements (see Figure 3 for examples), it is no longer appropriate to assume a single form of attenuation to rank templates or paired galaxies (Salim & Narayanan 2020).

The SED-fitting method allows attenuation curves to be obtained in a parametric form, but this method suffers from the well-known dust-age-metallicity degeneracy which may be alleviated by using IR data (Burgarella et al. 2005). More recently it is found that dust

attenuation curves can be constrained even without IR data (e.g. Kriek & Conroy 2013; Salim et al. 2016, 2018). However, by examining systematic biases in dust attenuation curves derived from SED modelling, Qin et al. (2022) concluded that the relation between the slope of dust attenuation curve and the optical depth found previously is likely caused by the degeneracy between model parameters. Lower et al. (2022) proposed a new method using a nonuniform screen dust model to allow a fraction of a galaxy to be unattenuated, and found a significant improvement in the dust attenuation modelling accuracy. Their finding again demonstrated the importance of using spatially resolved data.

Our method belongs to the second category. In our method we obtain the attenuation curve in the optical before applying our spectral fitting code BIGS to determine the stellar population properties, thus largely reducing the influence of the degeneracy between model parameters. The relation between the slope of dust attenuation curve and the optical depth is clearly seen in our sample (see Figure 7), suggesting that this relation is not entirely a result of systematic bias caused by degeneracy of model parameters as found in Qin et al. (2022). In addition, by applying our method to spatially resolved data, we have naturally taken into account the

non-uniform distribution of dust attenuation in galaxies, thus achieving higher accuracy in the dust attenuation measurements as found in Lower et al. (2022). Furthermore, by using NIR photometry to calibrate the absolute amplitude of the attenuation curves, we have taken a step forward in using the technique of Li et al. (2020) which provides only relative attenuation curves. Finally, by combining optical spectra from MaNGA and NUV photometry from *Swift*/UVOT, we have developed a novel method to estimate the 2175Å bump in attenuation curves. Clearly, our method can be tested and improved further using larger samples with broader wavelength coverage.

5.2. Comparison with previous observations

In the local Universe, previous studies have revealed a wide range of the attenuation curve slope, from those similar to the Calzetti curve to those steeper than the Milky Way extinction curve, as well as a trend of the curve slope with the optical opacity in the sense that galaxies with higher A_V tend to have shallower slopes. (e.g. Burgarella et al. 2005; Conroy et al. 2010; Wild et al. 2011; Battisti et al. 2016, 2017; Leja et al. 2017; Salim et al. 2018; Boquien et al. 2022; Nagaraj et al. 2022). In particular, using a sample of 23,000 galaxies with data from *GALEX*, SDSS and WISE, Salim & Narayanan (2020) showed that, once A_V is fixed, the slope- A_V relation does not show any significant residual dependence on the stellar mass, axis ratio, sSFR and stellar metallicity of the galaxies. The lack of dependence on stellar mass and sSFR was noticed by some earlier studies based on empirical methods (e.g. Johnson et al. 2007; Wild et al. 2011; Seon & Draine 2016). In our work, the slope- A_V anti-correlation and the lack of dependence on stellar mass, axis ratio and sSFR found earlier on galactic scales are also clearly seen at kpc scales (Figs. 5, 6 and 7), indicating that the global trends found previously originate from local regions at scales of kpc or smaller.

For the UV bump at 2175Å, previous studies of local galaxies based on the empirical method have not led to clear conclusions: with no/weak bump in some studies (e.g. Kinney et al. 1993; Calzetti et al. 1994, 2000; Battisti et al. 2016, 2017) and a moderate bump in others (e.g. Wild et al. 2011). In contrast, most of the studies based on SED-fitting techniques found evidence for a bump, with the strength ranging from zero to values close to or even higher than the MW's bump (e.g. Burgarella et al. 2005; Conroy et al. 2010; Salim et al. 2018). The results from Salim et al. (2018) supported the existence of a correlation between the curve slope and the bump strength, with weaker bumps in shallower curves.

A similar trend has also been found for high- z galaxies (e.g. Kriek & Conroy 2013). However, this correlation is not clearly seen in our result. As can be seen in Fig. 9, the bump strength shows no correlation with A_B/A_V ; it seems to slightly increase with the NUV slope, but the trend is rather weak. Note that in Kriek & Conroy (2013), the bump strength is tied to the slope of the curve by definition, which is different from other works in which a bump profile is simply added to the bump-free attenuation curve (e.g. Barišić et al. 2020; Kashino et al. 2021; Shivaie et al. 2022). Such a definition may induce a correlation between the bump strength and the curve slopes. Our method here does not rely on any specific attenuation curve, with the bump strength calculated in the *uvm2* band, which can also introduce minor differences in the derived properties. Cautions are urged when comparing different bump strength measurements. Apart from the detail differences, the strongest correlation we have found for the bump strength is with the sSFR (see Fig. 8), with B decreasing with increasing sSFR, and this correlation holds even when other properties are limited to narrow ranges. The same trend was previously reported by Kriek & Conroy (2013) and Kashino et al. (2021) for high- z galaxies based on global SED fitting. Shivaie et al. (2022) reported a similar but more complex trend such that the UV bump amplitude increases with mass at fixed SFR but does not change with SFR at fixed stellar mass. Again, our results indicate that the global trend seen previously is a result of the local trend present on kpc or smaller scales.

Our study is the first attempt to derive spatially-resolved dust attenuation curves and the UV bump strength for a sample of galaxies beyond the Local Group, though still with limited sample size (72 galaxies) and spatial resolution (\sim kpc). We note that the *Swift*/UVOT data have been used to study the spatial resolved dust attenuation curve and UV bump for a handful of nearby galaxies, e.g. M81 and Holmberg IX by Hoversten et al. (2011), SMC by Hagen et al. (2017) and NGC 628 by Declair et al. (2019). Both M81 and Holmberg IX can be best fit with a Milky Way extinction curve with a prominent UV bump, while the median attenuation curve of NGC 628 and SMC is fairly steep, with a sub-MW-type UV bump. In addition, intriguing variations are observed among different regions in NGC 628 and SMC, with regions of higher A_V found to have shallower attenuation curves and weaker UV bumps. Taking advantage of the wide ranges of galaxy properties covered by our sample, our study confirms those findings in case studies and investigate further the B -sSFR relation which was not seen clearly due to the

lack of spatially resolved spectroscopy and of a large sample.

5.3. What drives the variation in the 2175Å bump?

Although the exact carriers of the UV bump are still under debate, most of the studies agree that they should be some kind of carbonaceous grains with small sizes ($\lesssim 0.01\mu\text{m}$, Fischera & Dopita 2011). The production and destruction of the dust grains can thus affect the observed UV bump strength. In fact, many investigations went along this line to study the grain size distribution, and try to correlate the distribution with observed attenuation curves (e.g. Fischera & Dopita 2011; Asano et al. 2013; Hirashita & Murga 2020). For instance, Fischera & Dopita (2011) proposed that the ambient UV radiation field can destroy the carriers of the UV bump, and found that their models can naturally explain both the shallow slope and the absence of the UV bump for the Calzetti curve. Hirashita & Murga (2020) modelled the grain population by considering various dust components: silicate, aromatic carbon, and non-aromatic carbon, and found that their model can reproduce both the Milky Way and Calzetti curves by varying the star formation time scale and the dense gas fraction. Our finding that regions with higher sSFRs tend to have weaker UV bumps supports this scenario, as regions of intensive star formation produce strong UV photons that may destroy the bump carriers and thus reduce the bump strength. In the recent work of Kashino et al. (2021), where an anti-correlation between the bump strength and sSFR was also found for galaxies at $z \sim 0.8$, the bump variation was suggested to be determined by the recent star formation history of galaxies through the destruction of small carbonaceous grains by supernovae and intense radiation fields. A more recent work by Shivaeei et al. (2022) found that the UV bump strength highly correlates with the PAH strength indicated by the Spitzer MIPS 24 μm photometry, and that younger galaxies or galaxies that have experienced a recent (10-100 Myrs ago) starburst would have both reduced bump strengths and elevated mid-IR emission of PAHs.

On the other hand, even in the absence of the variation in the underlying dust grain properties and in the intrinsic dust extinction curve, the observed attenuation curve may still vary due to radiative transfer effects. For instance, Seon & Draine (2016) modelled the dust attenuation curves in a clumpy interstellar medium, and found that the attenuation curves are not necessarily determined by the underlying extinction curve. Instead, the absorption or scattering efficiency affects the shape of the curve, and the 2175Å bump from a MW extinction curve can be suppressed by using different albedos.

Similarly, Narayanan et al. (2018) combined the dust radiative transfer model with cosmological zoom-in simulations to show that the star-to-dust geometry alone can lead to the absence of the bump in the attenuation curve of a galaxy. Moreover, although different models give different explanations for the varying bump strength, they all predict flatter attenuation curves and weaker UV bumps for higher optical opacity. Since this prediction was in line with their findings for high- z galaxies at $0.5 < z < 2$, Kriek & Conroy (2013) suggested that the observed trends can be explained by differences in star-dust geometry, a varying grain size distribution, or both. By comparing galaxies in bins of sSFR and A_V in our sample, we found that the UV bump strength is more fundamentally anti-correlated with sSFR, while no obvious correlations with A_V are seen. In this regard, our result is actually not in favor of star-dust geometry as the driver for the UV bump variation. In addition, by using spatially-resolved data we have largely reduced the effect of the star-dust geometry, although the spatial resolution of our data is not high enough to fully resolve star-forming regions. Therefore, we argue that the variation of the UV bump can be more naturally explained by the first scenario, that is, destruction of dust grains to varying degrees due to varying UV photons produced by different star formation activities. Data with higher resolutions are needed to discriminate between different scenarios at sub-kpc scales, given that radiative transfer and geometry effects cannot be ignored at the MaNGA resolution.

6. SUMMARY

We have developed a novel method to measure the optical and NUV slopes as well as the 2175Å bump of dust attenuation curves at kpc scales for a sample of 72 galaxies in the local Universe, which have integral field spectroscopy from the MaNGA survey, NIR photometry in Ks band from 2MASS, and *Swift*/UVOT NUV photometry in uvw2, uvm2 and uvw1 bands from the SwiM catalog. For a given region in our sample, we first apply the technique of Li et al. (2020) to the MaNGA spectrum to derive a model-independent relative attenuation curve in the optical range ($A_\lambda - A_V$). Next, the observed spectrum from MaNGA is corrected for dust attenuation using the calibrated attenuation curve, and is fitted with our Bayesian inference code BIGS for stellar population synthesis to derive a dust-free model spectrum which extends to NUV and NIR. Finally, the dust-free spectrum is compared with the observed optical spectrum, 2MASS and the *Swift*/UVOT photometry, yielding the total attenuation in different bands (A_B , A_V , A_{w2} , A_{m2} , A_{w1}), the slope of the attenuation curve in both optical

(A_B/A_V) and NUV (A_{w2}/A_{w1}), and the strength of the 2175Å bump (B). We have applied this method to a set of mock spectra/SEDs with different SNRs, which are generated to cover a wide parameter space in stellar population and dust attenuation properties and mimic the quality of the data used in our study. This test shows that our method is able to well reproduce the average properties of dust attenuation in individual regions of our galaxies, with no/weak systematics and reasonably small errors.

We have examined the correlations of the dust attenuation parameters as measured in individual regions with the specific star formation rate (sSFR), as well as the correlations between the attenuation parameters themselves. We have also obtained *global* measurements of the dust attenuation parameters of individual galaxies, by applying the same method to the stacked spectrum and total photometry within the effective radius (R_e) of each galaxy. These measurements allow us to examine possible dependence of the dust attenuation laws on galaxy mass.

Our main results can be summarized as follows.

- Attenuation curves at kpc scales span a wide range of slopes in both optical and NUV, from those shallower than the Calzetti curve to those steeper than the Milky Way-type curves.
- The slope in both optical and NUV becomes shallower as one goes from low to high optical opacities, and this trend remains almost unchanged when the sample is limited to narrow ranges of sSFR, b/a , or the location within host galaxies.
- The 2175Å UV bump in regions of kpc scales presents a wide range of strengths, ranging from that of a Calzetti curve with no bump to those stronger than the bump in Milky Way-type curves.
- The 2175Å bump strength is primarily driven by sSFR with weaker bumps at higher sSFR, but not by the optical opacity, b/a and the location within host galaxies.
- The correlation between the 2175Å bump strength with sSFR instead of optical opacities strongly suggests that the UV bump variation is more fundamentally driven by processes related to star formation (e.g. destruction of dust grains by UV radiation in strongly star-forming regions).
- The above trends appear to be independent of the stellar mass of galaxies, indicating that the

dust attenuation laws are driven by local processes rather than by global properties of galaxies.

ACKNOWLEDGMENTS

This work is supported by the National Key R&D Program of China (grant No. 2018YFA0404502), and the National Science Foundation of China (grant Nos. 11821303, 11733002, 11973030, 11673015, 11733004, 11761131004, 11761141012). ME and CG acknowledge support from NASA grant 80NSSC20K0436. The work of MM is supported in part through a fellowship sponsored by the Willard L. Eccles Foundation. RY acknowledges support by the Hong Kong Global STEM Scholar Scheme, by the Hong Kong Jockey Club through the JC STEM Lab of Astronomical Instrumentation program, and by a grant from the Research Grant Council of the Hong Kong (Project No. 14302522).

Funding for SDSS-IV has been provided by the Alfred P. Sloan Foundation and Participating Institutions. Additional funding towards SDSS-IV has been provided by the US Department of Energy Office of Science. SDSS-IV acknowledges support and resources from the Centre for High-Performance Computing at the University of Utah. The SDSS web site is www.sdss.org.

SDSS-IV is managed by the Astrophysical Research Consortium for the Participating Institutions of the SDSS Collaboration including the Brazilian Participation Group, the Carnegie Institution for Science, Carnegie Mellon University, the Chilean Participation Group, the French Participation Group, Harvard-Smithsonian Center for Astrophysics, Instituto de Astrofísica de Canarias, The Johns Hopkins University, Kavli Institute for the Physics and Mathematics of the Universe (IPMU)/University of Tokyo, Lawrence Berkeley National Laboratory, Leibniz Institut für Astrophysik Potsdam (AIP), Max-Planck-Institut für Astronomie (MPIA Heidelberg), Max-Planck-Institut für Astrophysik (MPA Garching), Max-Planck-Institut für Extraterrestrische Physik (MPE), National Astronomical Observatory of China, New Mexico State University, New York University, University of Notre Dame, Observatorio Nacional/MCTI, The Ohio State University, Pennsylvania State University, Shanghai Astronomical Observatory, United Kingdom Participation Group, Universidad Nacional Autónoma de México, University of Arizona, University of Colorado Boulder, University of Oxford, University of Portsmouth, University of Utah, University of Virginia, University of Washington, University of Wisconsin, Vanderbilt University and Yale University.

REFERENCES

- Abdurro'uf, Accetta, K., Aerts, C., et al. 2022, *ApJS*, 259, 35, doi: [10.3847/1538-4365/ac4414](https://doi.org/10.3847/1538-4365/ac4414)
- Aguado, D. S., Ahumada, R., Almeida, A., et al. 2019, *ApJS*, 240, 23, doi: [10.3847/1538-4365/aaf651](https://doi.org/10.3847/1538-4365/aaf651)
- Asano, R. S., Takeuchi, T. T., Hirashita, H., & Nozawa, T. 2013, *MNRAS*, 432, 637, doi: [10.1093/mnras/stt506](https://doi.org/10.1093/mnras/stt506)
- . 2014, *MNRAS*, 440, 134, doi: [10.1093/mnras/stu208](https://doi.org/10.1093/mnras/stu208)
- Barišić, I., Pacifici, C., van der Wel, A., et al. 2020, *ApJ*, 903, 146, doi: [10.3847/1538-4357/abba37](https://doi.org/10.3847/1538-4357/abba37)
- Battisti, A. J., Calzetti, D., & Chary, R. R. 2016, *ApJ*, 818, 13, doi: [10.3847/0004-637X/818/1/13](https://doi.org/10.3847/0004-637X/818/1/13)
- . 2017, *ApJ*, 840, 109, doi: [10.3847/1538-4357/aa6fb2](https://doi.org/10.3847/1538-4357/aa6fb2)
- Battisti, A. J., Cunha, E. d., Shivaee, I., & Calzetti, D. 2020, *ApJ*, 888, 108, doi: [10.3847/1538-4357/ab5fdd](https://doi.org/10.3847/1538-4357/ab5fdd)
- Beegle, L. W., Wdowiak, T. J., Robinson, M. S., et al. 1997, *ApJ*, 487, 976, doi: [10.1086/304658](https://doi.org/10.1086/304658)
- Belfiore, F., Westfall, K. B., Schaefer, A., et al. 2019, *AJ*, 158, 160, doi: [10.3847/1538-3881/ab3e4e](https://doi.org/10.3847/1538-3881/ab3e4e)
- Blanton, M. R., Kazin, E., Muna, D., Weaver, B. A., & Price-Whelan, A. 2011, *AJ*, 142, 31, doi: [10.1088/0004-6256/142/1/31](https://doi.org/10.1088/0004-6256/142/1/31)
- Blanton, M. R., Bershad, M. A., Abolfathi, B., et al. 2017, *AJ*, 154, 28, doi: [10.3847/1538-3881/aa7567](https://doi.org/10.3847/1538-3881/aa7567)
- Boquien, M., Burgarella, D., Roehlly, Y., et al. 2019, *A&A*, 622, A103, doi: [10.1051/0004-6361/201834156](https://doi.org/10.1051/0004-6361/201834156)
- Boquien, M., Buat, V., Burgarella, D., et al. 2022, *A&A*, 663, A50, doi: [10.1051/0004-6361/202142537](https://doi.org/10.1051/0004-6361/202142537)
- Bradley, J., Dai, Z. R., Erni, R., et al. 2005, *Science*, 307, 244, doi: [10.1126/science.1106717](https://doi.org/10.1126/science.1106717)
- Bruzual, G., & Charlot, S. 2003, *MNRAS*, 344, 1000, doi: [10.1046/j.1365-8711.2003.06897.x](https://doi.org/10.1046/j.1365-8711.2003.06897.x)
- Buat, V., Giovannoli, E., Heinis, S., et al. 2011, *A&A*, 533, A93, doi: [10.1051/0004-6361/201117264](https://doi.org/10.1051/0004-6361/201117264)
- Buat, V., Noll, S., Burgarella, D., et al. 2012, *A&A*, 545, A141, doi: [10.1051/0004-6361/201219405](https://doi.org/10.1051/0004-6361/201219405)
- Buchner, J., Georgakakis, A., Nandra, K., et al. 2014, *A&A*, 564, A125, doi: [10.1051/0004-6361/201322971](https://doi.org/10.1051/0004-6361/201322971)
- Bundy, K., Bershad, M. A., Law, D. R., et al. 2015, *ApJ*, 798, 7, doi: [10.1088/0004-637X/798/1/7](https://doi.org/10.1088/0004-637X/798/1/7)
- Burgarella, D., Buat, V., & Iglesias-Páramo, J. 2005, *MNRAS*, 360, 1413, doi: [10.1111/j.1365-2966.2005.09131.x](https://doi.org/10.1111/j.1365-2966.2005.09131.x)
- Calzetti, D. 1997, *AJ*, 113, 162, doi: [10.1086/118242](https://doi.org/10.1086/118242)
- . 2001, *PASP*, 113, 1449, doi: [10.1086/324269](https://doi.org/10.1086/324269)
- Calzetti, D., Armus, L., Bohlin, R. C., et al. 2000, *ApJ*, 533, 682, doi: [10.1086/308692](https://doi.org/10.1086/308692)
- Calzetti, D., Kinney, A. L., & Storchi-Bergmann, T. 1994, *ApJ*, 429, 582, doi: [10.1086/174346](https://doi.org/10.1086/174346)
- Cardelli, J. A., Clayton, G. C., & Mathis, J. S. 1989, *ApJ*, 345, 245, doi: [10.1086/167900](https://doi.org/10.1086/167900)
- Chabrier, G. 2003, *PASP*, 115, 763, doi: [10.1086/376392](https://doi.org/10.1086/376392)
- Charlot, S., & Fall, S. M. 2000, *ApJ*, 539, 718, doi: [10.1086/309250](https://doi.org/10.1086/309250)
- Clayton, G. C., Gordon, K. D., Bianchi, L. C., et al. 2015, *ApJ*, 815, 14, doi: [10.1088/0004-637X/815/1/14](https://doi.org/10.1088/0004-637X/815/1/14)
- Conroy, C. 2013, *ARA&A*, 51, 393, doi: [10.1146/annurev-astro-082812-141017](https://doi.org/10.1146/annurev-astro-082812-141017)
- Conroy, C., Schiminovich, D., & Blanton, M. R. 2010, *ApJ*, 718, 184, doi: [10.1088/0004-637X/718/1/184](https://doi.org/10.1088/0004-637X/718/1/184)
- Declair, M., De Looze, I., Boquien, M., et al. 2019, *MNRAS*, 486, 743, doi: [10.1093/mnras/stz805](https://doi.org/10.1093/mnras/stz805)
- Driver, S. P., Andrews, S. K., da Cunha, E., et al. 2018, *MNRAS*, 475, 2891, doi: [10.1093/mnras/stx2728](https://doi.org/10.1093/mnras/stx2728)
- Drory, N., MacDonald, N., Bershad, M. A., et al. 2015, *AJ*, 149, 77, doi: [10.1088/0004-6256/149/2/77](https://doi.org/10.1088/0004-6256/149/2/77)
- Duffy, L., Molina, M., Eracleous, M., et al. 2023, *MNRAS*, doi: [10.1093/mnras/stad2722](https://doi.org/10.1093/mnras/stad2722)
- Eldridge, J. J., Stanway, E. R., Xiao, L., et al. 2017, *PASA*, 34, e058, doi: [10.1017/pasa.2017.51](https://doi.org/10.1017/pasa.2017.51)
- Faber, S. M. 1972, *A&A*, 20, 361
- Feroz, F., Hobson, M. P., & Bridges, M. 2009, *MNRAS*, 398, 1601, doi: [10.1111/j.1365-2966.2009.14548.x](https://doi.org/10.1111/j.1365-2966.2009.14548.x)
- Feroz, F., Hobson, M. P., Cameron, E., & Pettitt, A. N. 2013, *ArXiv e-prints*. <https://arxiv.org/abs/1306.2144>
- Fischera, J., & Dopita, M. 2011, *A&A*, 533, A117, doi: [10.1051/0004-6361/201116644](https://doi.org/10.1051/0004-6361/201116644)
- Fitzpatrick, E. L. 1999, *PASP*, 111, 63, doi: [10.1086/316293](https://doi.org/10.1086/316293)
- Gordon, K. D., Calzetti, D., & Witt, A. N. 1997, *ApJ*, 487, 625, doi: [10.1086/304654](https://doi.org/10.1086/304654)
- Gordon, K. D., & Clayton, G. C. 1998, *ApJ*, 500, 816, doi: [10.1086/305774](https://doi.org/10.1086/305774)
- Gordon, K. D., Clayton, G. C., Misselt, K. A., Landolt, A. U., & Wolff, M. J. 2003, *ApJ*, 594, 279, doi: [10.1086/376774](https://doi.org/10.1086/376774)
- Gunn, J. E., Siegmund, W. A., Mannery, E. J., et al. 2006, *AJ*, 131, 2332, doi: [10.1086/500975](https://doi.org/10.1086/500975)
- Hagen, L. M. Z., Siegel, M. H., Hoversten, E. A., et al. 2017, *MNRAS*, 466, 4540, doi: [10.1093/mnras/stw2954](https://doi.org/10.1093/mnras/stw2954)
- Hirashita, H. 2015, *MNRAS*, 447, 2937, doi: [10.1093/mnras/stu2617](https://doi.org/10.1093/mnras/stu2617)
- Hirashita, H., & Murga, M. S. 2020, *MNRAS*, 492, 3779, doi: [10.1093/mnras/stz3640](https://doi.org/10.1093/mnras/stz3640)
- Hoversten, E. A., Gronwall, C., Vanden Berk, D. E., et al. 2011, *AJ*, 141, 205, doi: [10.1088/0004-6256/141/6/205](https://doi.org/10.1088/0004-6256/141/6/205)
- Joblin, C., Leger, A., & Martin, P. 1992, *ApJL*, 393, L79, doi: [10.1086/186456](https://doi.org/10.1086/186456)

- Johnson, B. D., Leja, J. L., Conroy, C., & Speagle, J. S. 2019, *Prospector: Stellar population inference from spectra and SEDs*, Astrophysics Source Code Library, record ascl:1905.025. <http://ascl.net/1905.025>
- Johnson, B. D., Schiminovich, D., Seibert, M., et al. 2007, *ApJS*, 173, 392, doi: [10.1086/522960](https://doi.org/10.1086/522960)
- Jones, G. T., Stanway, E. R., & Carnall, A. C. 2022, *MNRAS*, 514, 5706, doi: [10.1093/mnras/stac1667](https://doi.org/10.1093/mnras/stac1667)
- Kashino, D., Lilly, S. J., Silverman, J. D., et al. 2021, *ApJ*, 909, 213, doi: [10.3847/1538-4357/abdf62](https://doi.org/10.3847/1538-4357/abdf62)
- Kauffmann, G., Heckman, T. M., White, S. D. M., et al. 2003, *MNRAS*, 341, 33, doi: [10.1046/j.1365-8711.2003.06291.x](https://doi.org/10.1046/j.1365-8711.2003.06291.x)
- Kennicutt, Jr., R. C. 1998, *ARA&A*, 36, 189, doi: [10.1146/annurev.astro.36.1.189](https://doi.org/10.1146/annurev.astro.36.1.189)
- Kinney, A. L., Bohlin, R. C., Calzetti, D., Panagia, N., & Wyse, R. F. G. 1993, *ApJS*, 86, 5, doi: [10.1086/191771](https://doi.org/10.1086/191771)
- Kinney, A. L., Calzetti, D., Bica, E., & Storchi-Bergmann, T. 1994, *ApJ*, 429, 172, doi: [10.1086/174309](https://doi.org/10.1086/174309)
- Kriek, M., & Conroy, C. 2013, *ApJL*, 775, L16, doi: [10.1088/2041-8205/775/1/L16](https://doi.org/10.1088/2041-8205/775/1/L16)
- Law, D. R., Yan, R., Bershady, M. A., et al. 2015, *AJ*, 150, 19, doi: [10.1088/0004-6256/150/1/19](https://doi.org/10.1088/0004-6256/150/1/19)
- Law, D. R., Cherinka, B., Yan, R., et al. 2016, *AJ*, 152, 83, doi: [10.3847/0004-6256/152/4/83](https://doi.org/10.3847/0004-6256/152/4/83)
- Law, D. R., Westfall, K. B., Bershady, M. A., et al. 2021, *AJ*, 161, 52, doi: [10.3847/1538-3881/abcaa2](https://doi.org/10.3847/1538-3881/abcaa2)
- Lawrence, A., Warren, S. J., Almaini, O., et al. 2007, *MNRAS*, 379, 1599, doi: [10.1111/j.1365-2966.2007.12040.x](https://doi.org/10.1111/j.1365-2966.2007.12040.x)
- Leja, J., Johnson, B. D., Conroy, C., van Dokkum, P. G., & Byler, N. 2017, *ApJ*, 837, 170, doi: [10.3847/1538-4357/aa5ffe](https://doi.org/10.3847/1538-4357/aa5ffe)
- Li, N., Li, C., Mo, H., et al. 2020, *ApJ*, 896, 38, doi: [10.3847/1538-4357/ab92a1](https://doi.org/10.3847/1538-4357/ab92a1)
- . 2021, *ApJ*, 917, 72, doi: [10.3847/1538-4357/ac0973](https://doi.org/10.3847/1538-4357/ac0973)
- Lower, S., Narayanan, D., Leja, J., et al. 2022, *ApJ*, 931, 14, doi: [10.3847/1538-4357/ac6959](https://doi.org/10.3847/1538-4357/ac6959)
- Maraston, C. 2005, *MNRAS*, 362, 799, doi: [10.1111/j.1365-2966.2005.09270.x](https://doi.org/10.1111/j.1365-2966.2005.09270.x)
- Martin, D. C., Fanson, J., Schiminovich, D., et al. 2005, *ApJL*, 619, L1, doi: [10.1086/426387](https://doi.org/10.1086/426387)
- Molina, M., Ajsaonkar, N., Yan, R., et al. 2020a, *MNRAS*, 494, 4751, doi: [10.1093/mnras/staa919](https://doi.org/10.1093/mnras/staa919)
- . 2020b, *ApJS*, 251, 11, doi: [10.3847/1538-4365/abba34](https://doi.org/10.3847/1538-4365/abba34)
- Nagaraj, G., Forbes, J. C., Leja, J., Foreman-Mackey, D., & Hayward, C. C. 2022, *ApJ*, 932, 54, doi: [10.3847/1538-4357/ac6c80](https://doi.org/10.3847/1538-4357/ac6c80)
- Narayanan, D., Conroy, C., Davé, R., Johnson, B. D., & Popping, G. 2018, *ApJ*, 869, 70, doi: [10.3847/1538-4357/aaed25](https://doi.org/10.3847/1538-4357/aaed25)
- Noll, S., Burgarella, D., Giovannoli, E., et al. 2009a, *A&A*, 507, 1793, doi: [10.1051/0004-6361/200912497](https://doi.org/10.1051/0004-6361/200912497)
- Noll, S., & Pierini, D. 2005, *A&A*, 444, 137, doi: [10.1051/0004-6361:20053635](https://doi.org/10.1051/0004-6361:20053635)
- Noll, S., Pierini, D., Pannella, M., & Savaglio, S. 2007, *A&A*, 472, 455, doi: [10.1051/0004-6361:20077067](https://doi.org/10.1051/0004-6361:20077067)
- Noll, S., Pierini, D., Cimatti, A., et al. 2009b, *A&A*, 499, 69, doi: [10.1051/0004-6361/200811526](https://doi.org/10.1051/0004-6361/200811526)
- Papoular, R. J., & Papoular, R. 2009, *MNRAS*, 394, 2175, doi: [10.1111/j.1365-2966.2009.14484.x](https://doi.org/10.1111/j.1365-2966.2009.14484.x)
- Papovich, C., Dickinson, M., & Ferguson, H. C. 2001, *ApJ*, 559, 620, doi: [10.1086/322412](https://doi.org/10.1086/322412)
- Qin, J., Zheng, X. Z., Fang, M., et al. 2022, *MNRAS*, 511, 765, doi: [10.1093/mnras/stac132](https://doi.org/10.1093/mnras/stac132)
- Reddy, N. A., Kriek, M., Shapley, A. E., et al. 2015, *ApJ*, 806, 259, doi: [10.1088/0004-637X/806/2/259](https://doi.org/10.1088/0004-637X/806/2/259)
- Rémy-Ruyer, A., Madden, S. C., Galliano, F., et al. 2014, *A&A*, 563, A31, doi: [10.1051/0004-6361/201322803](https://doi.org/10.1051/0004-6361/201322803)
- Roming, P. W. A., Kennedy, T. E., Mason, K. O., et al. 2005, *SSRv*, 120, 95, doi: [10.1007/s11214-005-5095-4](https://doi.org/10.1007/s11214-005-5095-4)
- Salim, S., Boquien, M., & Lee, J. C. 2018, *ApJ*, 859, 11, doi: [10.3847/1538-4357/aabf3c](https://doi.org/10.3847/1538-4357/aabf3c)
- Salim, S., & Narayanan, D. 2020, *ARA&A*, 58, 529, doi: [10.1146/annurev-astro-032620-021933](https://doi.org/10.1146/annurev-astro-032620-021933)
- Salim, S., Charlot, S., Rich, R. M., et al. 2005, *ApJL*, 619, L39, doi: [10.1086/424800](https://doi.org/10.1086/424800)
- Salim, S., Rich, R. M., Charlot, S., et al. 2007, *ApJS*, 173, 267, doi: [10.1086/519218](https://doi.org/10.1086/519218)
- Salim, S., Lee, J. C., Janowiecki, S., et al. 2016, *ApJS*, 227, 2, doi: [10.3847/0067-0049/227/1/2](https://doi.org/10.3847/0067-0049/227/1/2)
- Savage, B. D. 1975, *ApJ*, 199, 92, doi: [10.1086/153668](https://doi.org/10.1086/153668)
- Sawicki, M., & Yee, H. K. C. 1998, *AJ*, 115, 1329, doi: [10.1086/300291](https://doi.org/10.1086/300291)
- Scoville, N., Faisst, A., Capak, P., et al. 2015, *ApJ*, 800, 108, doi: [10.1088/0004-637X/800/2/108](https://doi.org/10.1088/0004-637X/800/2/108)
- Seon, K.-I., & Draine, B. T. 2016, *ApJ*, 833, 201, doi: [10.3847/1538-4357/833/2/201](https://doi.org/10.3847/1538-4357/833/2/201)
- Shivaei, I., Reddy, N., Rieke, G., et al. 2020, *ApJ*, 899, 117, doi: [10.3847/1538-4357/aba35e](https://doi.org/10.3847/1538-4357/aba35e)
- Shivaei, I., Boogaard, L., Díaz-Santos, T., et al. 2022, *MNRAS*, 514, 1886, doi: [10.1093/mnras/stac1313](https://doi.org/10.1093/mnras/stac1313)
- Skrutskie, M. F., Cutri, R. M., Stiening, R., et al. 2006, *AJ*, 131, 1163, doi: [10.1086/498708](https://doi.org/10.1086/498708)
- Smee, S. A., Gunn, J. E., Uomoto, A., et al. 2013, *AJ*, 146, 32, doi: [10.1088/0004-6256/146/2/32](https://doi.org/10.1088/0004-6256/146/2/32)
- Spinrad, H., & Taylor, B. J. 1971, *ApJS*, 22, 445, doi: [10.1086/190232](https://doi.org/10.1086/190232)

- Stecher, T. P. 1965, *ApJ*, 142, 1683, doi: [10.1086/148462](https://doi.org/10.1086/148462)
- Steglich, M., Jäger, C., Rouillé, G., et al. 2010, *ApJL*, 712, L16, doi: [10.1088/2041-8205/712/1/L16](https://doi.org/10.1088/2041-8205/712/1/L16)
- Vazdekis, A., Sánchez-Blázquez, P., Falcón-Barroso, J., et al. 2010, *MNRAS*, 404, 1639, doi: [10.1111/j.1365-2966.2010.16407.x](https://doi.org/10.1111/j.1365-2966.2010.16407.x)
- Wake, D. A., Bundy, K., Diamond-Stanic, A. M., et al. 2017, *AJ*, 154, 86, doi: [10.3847/1538-3881/aa7ecc](https://doi.org/10.3847/1538-3881/aa7ecc)
- Westfall, K. B., Cappellari, M., Bershady, M. A., et al. 2019, *AJ*, 158, 231, doi: [10.3847/1538-3881/ab44a2](https://doi.org/10.3847/1538-3881/ab44a2)
- Wild, V., Charlot, S., Brinchmann, J., et al. 2011, *MNRAS*, 417, 1760, doi: [10.1111/j.1365-2966.2011.19367.x](https://doi.org/10.1111/j.1365-2966.2011.19367.x)
- Witt, A. N., & Gordon, K. D. 2000, *ApJ*, 528, 799, doi: [10.1086/308197](https://doi.org/10.1086/308197)
- Wright, E. L., Eisenhardt, P. R. M., Mainzer, A. K., et al. 2010, *AJ*, 140, 1868, doi: [10.1088/0004-6256/140/6/1868](https://doi.org/10.1088/0004-6256/140/6/1868)
- Yan, R., Tremonti, C., Bershady, M. A., et al. 2016a, *AJ*, 151, 8, doi: [10.3847/0004-6256/151/1/8](https://doi.org/10.3847/0004-6256/151/1/8)
- Yan, R., Bundy, K., Law, D. R., et al. 2016b, *AJ*, 152, 197, doi: [10.3847/0004-6256/152/6/197](https://doi.org/10.3847/0004-6256/152/6/197)
- York, D. G., Adelman, J., Anderson, Jr., J. E., et al. 2000, *AJ*, 120, 1579, doi: [10.1086/301513](https://doi.org/10.1086/301513)
- Zeimann, G. R., Ciardullo, R., Gronwall, C., et al. 2015, *ApJ*, 814, 162, doi: [10.1088/0004-637X/814/2/162](https://doi.org/10.1088/0004-637X/814/2/162)
- Zhou, S., Li, C., Hao, C.-N., et al. 2021, *ApJ*, 916, 38, doi: [10.3847/1538-4357/ac06cc](https://doi.org/10.3847/1538-4357/ac06cc)
- Zhou, S., Mo, H. J., Li, C., Boquien, M., & Rossi, G. 2020, *MNRAS*, 497, 4753, doi: [10.1093/mnras/staa2337](https://doi.org/10.1093/mnras/staa2337)
- Zhou, S., Mo, H. J., Li, C., et al. 2019, *MNRAS*, 485, 5256, doi: [10.1093/mnras/stz764](https://doi.org/10.1093/mnras/stz764)